International Journal of Fracture **124:** 43–77, 2003.

Strain localization at the crack tip in single crystal CT specimens under monotonous loading: 3D Finite Element analyses and application to nickel-base superalloys

S. FLOURIOT[1], S. FOREST[1,*], G. CAILLETAUD[1], A. KÖSTER[1], L. RÉMY[1], B. BURGARDT[2], V. GROS[2], S. MOSSET[2] and J. DELAUTRE[2]
[1]*Centre des Matériaux/UMR 7633, Ecole des Mines de Paris/CNRS, BP 87, 91003 Evry Cedex, France (*Author for correspondence: E-mail: samuel.forest@mat.ensmp.fr)*
[2]*SNECMA moteurs, Villaroche, 77550 Moissy Cramayel, France*

Received 4 March 2003; accepted in revised form 1 October 2003

Abstract. Three-dimensional Finite Element simulations of mode I crack tip fields in Compact Tension specimens are presented for elastic ideally-plastic F.C.C. single crystals. The computations are carried out within the framework of classical continuum crystal plasticity for three crack orientations: (001)[110], (110)[001] and (001)[100]. The attention is drawn on the strong differences between the plastic strain field obtained at the free surface and in the mid-section of the specimens. The results are compared, on the one hand, to analytical solutions for stationary cracks in single crystals under plane strain conditions and, on the other hand, to experimental tests on a single crystal nickel-based superalloy at room temperature. For this material, both octahedral and cube slip must be taken into account. A good agreement between experimental observations and numerical results is found in the structure of the strain localization bands observed at the free surface of (110)[001] cracked specimens. In particular, the evidence of kink banding near the crack tip is provided, confirmed by EBSD orientation mapping. The measured values of local lattice rotation are in agreement with the Finite Element prediction.

Key words: Continuum crystal plasticity, crack tip, electron back-scattered diffraction (EBSD), finite element, localization, Ni-base superalloys, single crystal.

1. Introduction

The determination of stress and strain fields at the crack tip in single crystals is an essential step towards the prediction of subsequent crack growth in crystalline solids or single crystalline structures under monotonous or cyclic loading. The analysis of crack tip stress fields in anisotropic ideally-plastic materials goes back to the work of Pan (1986). Rice (1987) proposed the first asymptotic solution of the crack tip stress field in F.C.C. and B.C.C. single crystals for two specific crack orientations under plane strain conditions and using a small strain plasticity framework. The solution has even been extended to hexagonal (H.C.P.) crystals including two slip system families, prismatic and pyramidal ones (Gupta, 1993). Rice's solution can be extended to power–law hardening crystals, as done in (Saeedvafa and Rice, 1989).

Finite Element simulations are then necessary to consider more general kinematic conditions and specimen geometry, but also more complex constitutive equations. The two–dimensional Finite Element simulations reported in (Rice et al., 1990; Cuitiño and Ortiz, 1992; Mohan et al., 1992) are consistent with the asymptotic analyses under mode I and III loading conditions, and provide new insight in the case of hardening crystals within the finite strain

framework, therefore including lattice rotation. The analysis of real fracture mechanics specimens like notched beams or Compact Tension (CT) samples requires full three-dimensional analyses in order to evaluate the usual plane strain condition at the specimen center and to determine the stress-strain fields at free surfaces. To the author's knowledge, the only available three-dimensional Finite Element solutions of crack tip plasticity in single crystals are to be found in Cuitiño and Ortiz' (1996) work. In the case of notched four-point bending copper specimens, they brought to the attention the fact that the strain field observed at the free surface of the specimen may strongly differ from the response in the bulk depending on crystal orientations.

From the physical metallurgical view point, the mechanisms of fatigue crack growth in single crystals are well–documented since the pioneering works of Garret (1975) and Neumann (1974) in aluminium. However, one had to wait until the early 1990s to get a precise picture of slip system activity around the crack tip in single crystals (Cho and Yu, 1991; Shield and Kim, 1994; Shield, 1996). Experimental techniques for determination of near-tip deformation field rely on surface measurements like Moiré interferometry. Crone and Shield (2001) have presented detailed observations of the deformation near a notch tip in copper and copper-beryllium single crystals. They compare their results obtained on the surface of the specimens with Rice's two-dimensional analytical solutions and Cuitiño and Ortiz three-dimensional Finite Element results. Experimental measurements in the core of the specimens are more difficult since slip lines cannot be seen. Another quantity remains observable however even after cutting the specimen into pieces: lattice rotation observed by Electron Back–Scatter Diffraction (EBSD). This has been done recently by Kysar and Briand (2002), who were able to show the existence of so-called kink bands near the crack tip of aluminium crystals. This concept will be explained in more details in Section 2.3 of this work.

The importance of previous analyses for industrial applications becomes clear when one thinks of structures like blades in high pressure turbines of jet engines (Méric et al., 1991). Such components are subjected to severe thermomechanical loading conditions. That is why they are made of single crystal nickel-base superalloys that exhibit an outstanding creep-fatigue behaviour from room temperature up to more than 1000 °C (Rémy and Skelton, 1992). The fatigue crack growth in single crystal nickel-base superalloys has been investigated at many places, especially its orientation dependence (Leverant and Gell, 1975; Crompton and Martin, 1984a, b; Aswath, 1994). As early as 1984, Crompton was able to estimate experimentally the extension of the plastic zone around cracks in single crystal superalloys. Compact Tension (CT) specimens were used in (Lerch and Antolovich, 1990; Fleury, 1991) and (Henderson and Martin, 1996) to study fatigue crack growth in the single crystal nickel-base superalloys SRR99, René 4 and AM1 from room temperature to 850 °C or even 1100 °C. Another specimen geometry (Single Edge Notched (SEN) samples) were used by Defresne and Rémy (1990) to investigate initiation and propagation of fatigue cracks in CMSX2 single crystal superalloy. The crystallographic structure of single crystal nickel-base superalloys is F.C.C. A peculiar feature of the plasticity of this material is that it relies not only on usual octahedral slip with respect to $\{111\}$ planes but also on cube slip with respect to $\{001\}$ planes. This must be taken into account when analysing crack tip fields in nickel-base superalloys. Single crystal nickel-base superalloys display an almost elastic-ideally-plastic behaviour in tension at low temperature. They are therefore good candidates for experimental validation of available analytical solutions of the crack tip problem. More information on the deformation of single crystals nickel-base superalloys is postponed to Section 2.1.

The aim of the present work is to provide fully three-dimensional Finite Element analyses of the near-tip stress–strain fields in Compact Tension specimens in elastic ideally-plastic single crystals for three different orientations. The analysis is applied to the specific case of single crystal nickel-base superalloy AM1 at low temperature. Experimental results on CT specimens are then compared with numerical simulations in order to evaluate the relevance of the used classical continuum crystal plasticity framework (Asaro, 1983).

Section 2 recalls the main features of the asymptotic solution for the stress field around a crack tip in elastic ideally-plastic single crystals. The methodology is applied to the specific case of single crystal nickel-base superalloys for which both octahedral and cube slip systems must be taken into account. Three crack orientations with respect to the crystal are considered throughout this work: (001)[110], (110)[001] and (001)[100]. The first plane ( ) denotes the crack plane and the direction [ ] the crack propagation direction. This convention is used throughout this work. The continuum crystal plasticity Finite Element model and computational tools are presented in Section 3. The used 2D and 3D Finite Element meshes of the considered CT specimens are described in detail. The simulation of large 3D meshes has been made possible by resorting to parallel computing. Section 4 is devoted to the numerical results. The three-dimensional plastic strain fields around the crack tip in CT specimens are described in detail and compared to the 2D solution. The experimental results on three single crystal nickel-base CT specimens are reported in Section 5. The stress is laid on the identification of the slip lines observed near the crack tip and to EBSD measurements. In the final discussion, the Finite Element results are explicitely compared to the available experimental observations.

2. Stress-strain field at the crack tip under plane strain conditions

2.1. Presentation of the material

Single crystal nickel base superalloy AM1 is used for high temperature turbine blade applications in jet engines. Its chemical composition can be found in (Hanriot et al., 1991). Three successive thermal treatments are needed to produce the adequate microstructure that improves the creep properties of the material. Two phases are present in the material. The γ matrix is a F.C.C. disordered phase whereas the γ' precipitates have an ordered $L1_2$ F.C.C. crystallographic structure. The volume fraction of precipitates is about 70%. They have a regular spatial distibution and a cuboidal shape with a side of about 0.5 μm. The lattices of matrix and precipitates are coherent with a slight misfit, so that the material remains a single crystal as can be seen from X-ray or EBSD analysis.

The thermomechanical properties of this material have been extensively studied regarding tension, fatigue and creep behaviour and damage (Méric et al., 1991; Hanriot et al., 1991; Köster and Rémy, 2000). They can be compared to similar nickel-base single crystal superalloys used for jet engine applications (Rémy and Skelton, 1992; Defresne and Rémy, 1990). The present work is restricted to the low–temperature behaviour of the material because it is nearly elastic-perfectly plastic at least under monotonous loading, and prone to strain localization into intense slip bands (Flouriot et al., 2003). The investigated temperatures are room temperature and 650 °C. Under these conditions plastic deformation results from cristallographic slip on the slip plane defined by its normal vector $\underline{\mathbf{n}}^s$ along the glide direction $\underline{\mathbf{l}}^s$ for the slip system s. Tension along $\langle 001 \rangle$ crystallographic direction reveals the presence of octahedral slip as expected in F.C.C. materials. Twelve octahedral slip systems must be taken into account. The slip planes are $\{111\}$ and the slip directions $\langle 011 \rangle$. In contrast, the slip

Table 1. Material parameters for single crystal nickel-base superalloy AM1 at room temperature and 650 °C.

Temperature	Elasticity (MPa)			Octahedral			Cube		
	C_{11}	C_{12}	C_{44}	n	k (MPa$^{1/n}$)	τ_c (MPa)	n	k (MPa$^{1/n}$)	τ_c (MPa)
20 °C	296000	204000	125000	10	0.1	245	10	0.1	377
650°C	244000	170000	104000	10	0.1	204	10	0.1	170

lines observed on specimens in tension along ⟨111⟩ directions are traces of cube planes. This activation of cube slip has been reported in many single crystal nickel-base superalloys (Méric et al., 1991; Hanriot et al., 1991; Bettge and Osterle, 1999; Arakere and Swanson, 2002). There are six cube slip systems, with slip planes {001} and slip directions ⟨110⟩. The Schmid law has been shown to be a well-suited yield criterion in order to predict the activation of octahedral and cube slip (Méric et al., 1991), at least in the plastic strain and strain rate ranges investigated in this work. This fact has been confirmed even under multiaxial loading conditions, namely tension–compression–torsion of single crystals (Nouailhas et al., 1993; Nouailhas and Cailletaud, 1995; Forest et al., 1996). The initial critical resolved shear stresses τ_c for the octahedral and cube slip system families are different and depend on temperature. They are reported in Table 1 for the temperatures investigated in this work. No subsequent hardening is introduced in this work at these temperatures, except otherwise stated. In particular, no interaction between slip systems is accounted for.

2.2. Asymptotic analyses at the crack tip

Rice (1987) performed an asymptotic analysis of the plane-strain stress field at a crack tip in elastic-ideally plastic F.C.C. and B.C.C. single crystals. He considered (001)[110] and (110)[001] crack orientations for both F.C.C. and B.C.C. single crystals. The same analysis is possible for the crack orientation (001)[100] as shown in (Flouriot et al., 2003). In the present work, Cartesian axes $(\underline{\mathbf{x}}_1, \underline{\mathbf{x}}_2, \underline{\mathbf{x}}_3)$ are introduced. The crack plane is assumed to be perpendicular to $\underline{\mathbf{x}}_2$ and the crack propagation direction is parallel to $\underline{\mathbf{x}}_1$. Accordingly, the crack front is parallel to $\underline{\mathbf{x}}_3$. The enforced plain strain conditions are $\varepsilon_{33} = \varepsilon_{23} = \varepsilon_{13} = 0$. The considered anisotropic yield criterion is Schmid's law saying that plastic flow can occur for slip system s only when the resolved shear stress τ^s reaches a critical value τ_c:

$$\tau^s = \underset{\sim}{\boldsymbol{\sigma}} : \underset{\sim}{\mathbf{m}}^s = \tau_c \quad \text{with} \quad \underset{\sim}{\mathbf{m}}^s = \tfrac{1}{2}\left(\underline{\mathbf{l}}^s \otimes \underline{\mathbf{n}}^s + \underline{\mathbf{n}}^s \otimes \underline{\mathbf{l}}^s\right). \tag{1}$$

For the (001)[110] and (110)[001] cracks, only three pairs of simultaneously activated slip systems can produce sustained plane strain flow (Rice, 1987). Each pair can be regarded as an effective slip system with one slip plane trace on the $(\underline{\mathbf{x}}_1, \underline{\mathbf{x}}_2)$ plane. Let $\underline{\mathbf{S}}[= (S_1, S_2, 0)]$ be a unit vector parallel to one of these slip plane traces. For both considered crack orientations, the three possible directions for $\underline{\mathbf{S}}$ are $\theta = 0, 54.7°, 125.3°$. The unit vector normal to $\underline{\mathbf{S}}$ contained in the $(\underline{\mathbf{x}}_1, \underline{\mathbf{x}}_2)$ plane is called $\underline{\mathbf{N}}$.

The application of Schmid's law on the three effective slip systems leads to a hexagonal yield locus in the $(\sigma_{11} - \sigma_{22})/2$ versus σ_{12} plane. Each side of the yield surface corresponds to plane strain shear on one of the three effective slip systems. As discussed by Rice (1987) it is convenient to describe the yield surface in terms of the geometry of these effective slip

systems, that is the vectors $\underline{\mathbf{S}}$ and $\underline{\mathbf{N}}$. Then the yield condition associated with this slip system can be written as

$$N_\alpha \sigma_{\alpha\beta} S_\beta = \pm\beta\tau_c, \tag{2}$$

where Greek indices range over 1,2 only. The coefficient β is related to the Schmid factor associated with each effective slip system. One may rewrite this equation in the following form (since $S_1 = N_2$, $S_2 = -N_1$)

$$2N_1N_2\frac{\sigma_{11} - \sigma_{22}}{2} + (N_2^2 - N_1^2)\sigma_{12} = \pm\beta\tau_c. \tag{3}$$

Let now (r, θ) be polar coordinates centered at the crack tip. All bounded crack tip stress states must then satisfy the equilibrium condition :

$$\sigma'_{\alpha\beta} = e_\alpha e_\beta(\sigma'_{11} + \sigma'_{22}). \tag{4}$$

Here $e_\alpha = \partial r/\partial x_\alpha$ with $(e_1, e_2) = (\cos\theta, \sin\theta)$ the radial unit vector in the $(\underline{\mathbf{x}}_1, \underline{\mathbf{x}}_2)$ plane, while $e'_\alpha = \partial e_\alpha/\partial\theta$ is the unit vector normal to e_α contained in the $(\underline{\mathbf{x}}_1, \underline{\mathbf{x}}_2)$ plane in the direction of increasing θ. Lastly, $\sigma'_{ij} = \sigma'_{ij}(\theta)$ denotes

$$\sigma'_{ij} = \lim_{r\to 0}\left[\frac{\partial\sigma_{ij}(r,\theta)}{\partial\theta}\right]. \tag{5}$$

In a particular angular sector at yield, Equation (2) must be satisfied. Combined with (4), it requires that

$$(N_\alpha e_\alpha)(S_\lambda e_\lambda)(\sigma'_{11} - \sigma'_{22}) = 0. \tag{6}$$

Thus, Equation (6) implies that the stress (as $r \to 0$) in angular sectors which are at yield must be constant (independant of θ) except for special values of θ for which the radial vector $\underline{\mathbf{e}}$ coincides with $\underline{\mathbf{S}}$ or $\underline{\mathbf{N}}$. For these special values the stresses change discontinuously, provided that plastic loading occurs in all sectors. This last assumption is that of the stationary crack investigated by Rice (1987) and in the present work. Suppose then that a stress jump $[\![\sigma_{\alpha\beta}]\!] \neq 0$ exists on a ray of direction $\underline{\mathbf{e}}$ ($[\![f]\!] = f(\theta^+) - f(\theta^-)$). The continuity of the traction vector across the ray requires that

$$e'_\alpha [\![\sigma_{\alpha\beta}]\!] = 0 \tag{7}$$

or, equivalently,

$$[\![\sigma_{\alpha\lambda}]\!] = e_\alpha e_\lambda [\![\sigma_{11} + \sigma_{22}]\!]. \tag{8}$$

The solution consistent with these discontinuity requirements is such that the stress state must change from vertex to vertex of the yield surface at a discontinuity. That is why the last equation for the jump of the sum of the in-plane principal stresses involves the arc length L around the yield locus, having the unit of stress and increasing in the counterclockwise sense:

$$[\![\tfrac{1}{2}(\sigma_{11} + \sigma_{22})]\!] = -[\![L]\!]. \tag{9}$$

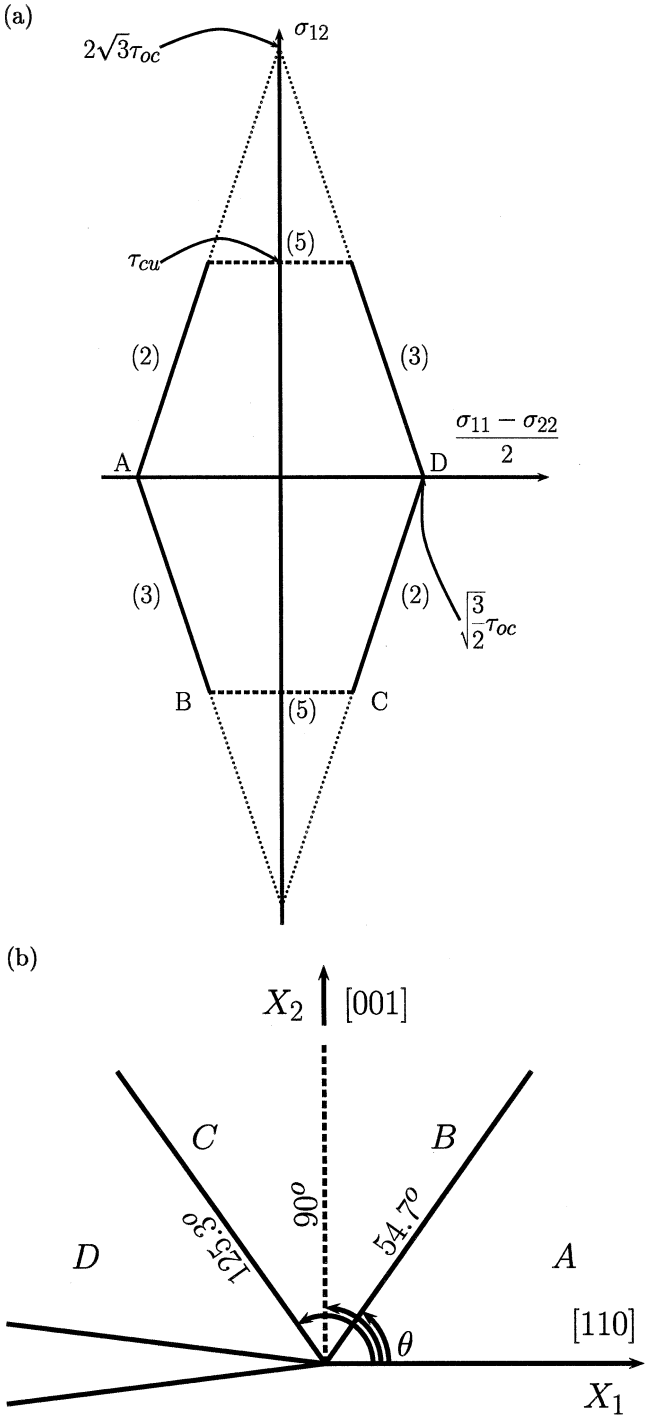

Figure 1. Structure of the crack tip field solution for the (001)[110] crack orientation: (a) yield surface, τ_{oc} and τ_{cub} being the critical resolved shear stresses for octahedral and cube slip respectively (see Table 1); (b) sector boundaries, the rays with given angle θ correspond to stress discontinuity. The Cartesian components of the stress tensor are constant in the sectors labelled A to D. The yield surface edges and sector boundary corresponding to the activation of cube slip are in dashed lines.

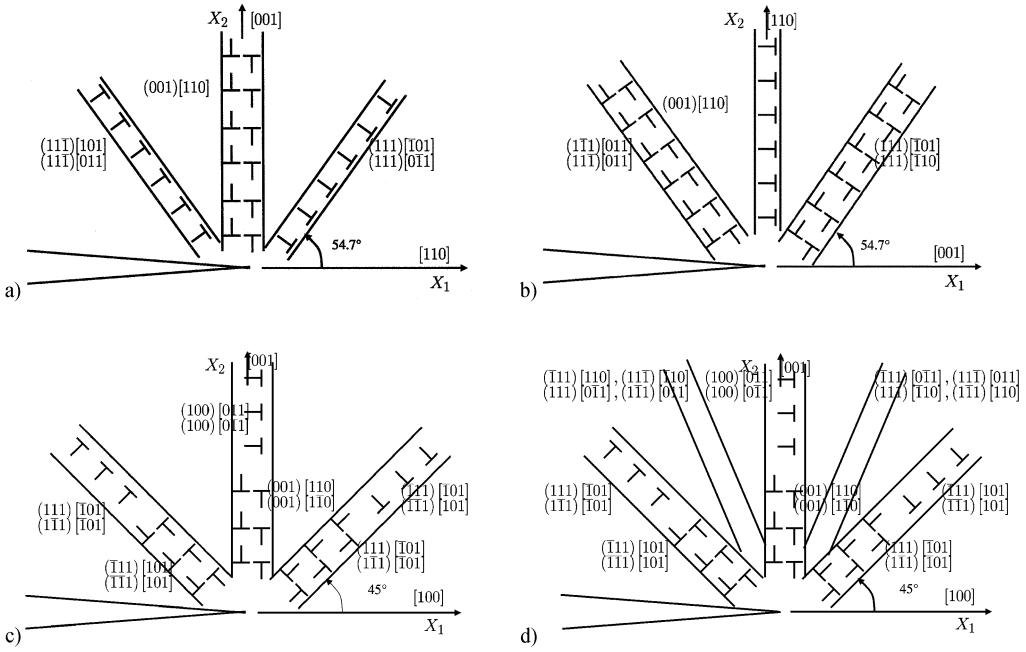

Figure 2. Structure of the discontinuity lines interpreted as slip, kink or more complex bands: (a) (001)[110] crack, (b) (110)[001] crack, (c) (001)[100] crack when $\rho < \sqrt{3}/2$, (d) [001](100) crack when $\sqrt{3}/2 < \rho < \sqrt{3}$.

We follow now the same reasoning in the case of two slip system families in F.C.C. crystals, namely octahedral and cube slip systems. Three crack orientations are considered successively.

2.2.1. (001)[110] *and* (110)[001] *cracks*

The yield surface depends on the ratio of the critical resolved shear stresses for octahedral and cube slip systems $\rho = \tau_{cub}/\tau_{oc}$. If ρ is greater than $\sqrt{3}$, cube slip systems cannot be activated prior to octahedral ones, so that the previous solution is still valid. If ρ is less than $\sqrt{3}$ the global shape of the yield surface is unchanged (see Figure 1a). It is still an hexagonal yield surface, but the horizontal line on the yield surface corresponds to the activation of the cube slip system (001)[110] (this is the notation for slip systems used throughout this work: the first plane is the slip plane, the second vector is the slip direction). There are again three groups of slip systems that are able to produce plane strain plastic flow:

$$\{(11\overline{1})[101];\ (11\overline{1})[011]\},\ \{(001)[110]\},\ \{(111)[\overline{1}01];\ (111)[0\overline{1}1]\}$$

One of this group reduces to the single slip system (001)[110]. Again, a solution exists with sectors of constant stress states bounded by discontinuity lines having the same angles as in Rice's original solution. The sectors are shown in Figure 1b. The geometrical structure of the crack tip solution is the same for both (001)[110] and (110)[001] cracks.

The discontinuity lines can also be interpreted in practice as strain localization bands (Forest et al., 2001). The type of bands differs for (001)[110] and (110)[001] cracks as shown in Figure 2a. For the (001)[110] crack, the inclined bands AB or CD (the notation AB means the discontinuity between sectors A and B) are parallel to the common slip plane of the pair $\{(11\overline{1})[101]);\ (11\overline{1})[011]\}$ and the resulting slip direction [112] is also parallel to the discontinuity line. That is why it can be called an effective slip band. In contrast, in the

vertical band the slip plane is horizontal and so does the slip direction. This is usually called a kink band (Rice et al., 1990) (see also (Gilman, 1955) for kink bands in H.C.P. single crystals). Note that such a kink configuration is associated with lattice rotation contrary to the case of slip bands. This lattice rotation is however not taken into account in the asymptotic analysis. It will be incorporated in the Finite Element analyses provided in this work. The inverse situation is met for the (110)[001] crack: the inclined bands are kinks whereas the vertical one is an effective slip band (Figure 2b).

2.2.2. (001)[100] *crack*

An asymptotic solution under plane strain conditions also exists in the case of a (001)[100] crack. It has been established in (Flouriot et al., 2003) in the case of pure octahedral slip. The yield locus also is an hexagon but with two sides parallel to the σ_{12} axis. Combinations of four slip systems lead to effective slip systems consistent with plane strain conditions. Three groups of slip systems are pointed out:

$$\{(111)[\bar{1}01];\ (1\bar{1}1)[\bar{1}01];\ (\bar{1}11)[101];\ (\bar{1}\bar{1}1)[101]\},$$

$$\{(111)[0\bar{1}1];\ (11\bar{1})[\bar{1}10];\ (\bar{1}11)[110];\ (1\bar{1}1)[011]\},$$

$$\{(\bar{1}11)[0\bar{1}1];\ (11\bar{1})[011];\ (111)[\bar{1}10];\ (1\bar{1}1)[110]\}.$$

Along half a circle around the crack tip, for θ varying from 0 to 180°, the stress state follows four adjacent edges of the yield locus, which results in four discontinuity lines. The yield locus, sectors and discontinuity lines are given in (Flouriot et al., 2003) for octahedral slip only.

The previous solution can be modified to incorporate both octahedral and cube slip. In this case, four combinations of slip systems can produce plane strain plastic flow, namely the three previous combinations and the following additional one:

$$\{(100)[011];\ (100)[01\bar{1}];\ (001)[110];\ (001)[1\bar{1}0]\}.$$

However, the activation of these potential effective systems depends on the ratio $\rho = \tau_{cub}/\tau_{oc}$. If ρ is less than $\sqrt{3}/2$ then the yield surface has the rectangular shape shown in Figure 3a. This is the case for AM1 at 650 °C according to Table 1. As a result, the mode I crack tip field admits four constant stress sectors (Figure 3b). The corresponding stress values are given in Table 2. The structure of the strain localization bands associated with the three discontinuity lines is detailed in Figure 2c. Four slip systems are activated simultaneously in each band, cube systems in the vertical band and octahedral ones in the inclined bands. The band inclined at 45° (respectively, 135°) can be interpreted as superimposed effective $(\bar{1}01)[101]$ slip (respectively, kink) band and $(101)[\bar{1}01]$ kink (respectively, slip) band. The vertical band is made of superimposed effective (001)[100] kink band and (100)[001] slip band.

When $\sqrt{3}/2 < \rho < \sqrt{3}$, the yield locus has the octagonal shape drawn in Figure 4a. In that case all four effective slip systems listed above are activated and distributed into six sectors, as shown in Figure 4. The corresponding stress levels are given in Table 3. The structure of the five strain localization bands associated with the discontinuity lines is described in Figure 2d. The two additional bands at 67.5° and 112.5° have a more complex structure than the three others and cannot be interpreted as superimposed pure slip and kink bands (see also Forest et al., 2001; Flouriot et al., 2003).

Table 2. Stress values in the sectors around the tip of a stationary (001)[100] crack, in the case $\tau_{cub}/\tau_{oc} < \sqrt{3}/2$. The sector names are indicated in the corresponding Figure 3.

Sector	σ_{11}	σ_{22}	σ_{12}
A	$\sqrt{6}\tau_{oc} + 2\sqrt{2}\tau_{cu}$	$2\sqrt{6}\tau_{oc} + 2\sqrt{2}\tau_{cu}$	0
B	$\sqrt{6}\tau_{oc} + \sqrt{2}\tau_{cu}$	$2\sqrt{6}\tau_{oc} + \sqrt{2}\tau_{cu}$	$-\sqrt{2}\tau_{cu}$
C	$\sqrt{6}\tau_{oc} + \sqrt{2}\tau_{cu}$	$\sqrt{2}\tau_{cu}$	$-\sqrt{2}\tau_{cu}$
D	$\sqrt{6}\tau_{oc}$	0	0

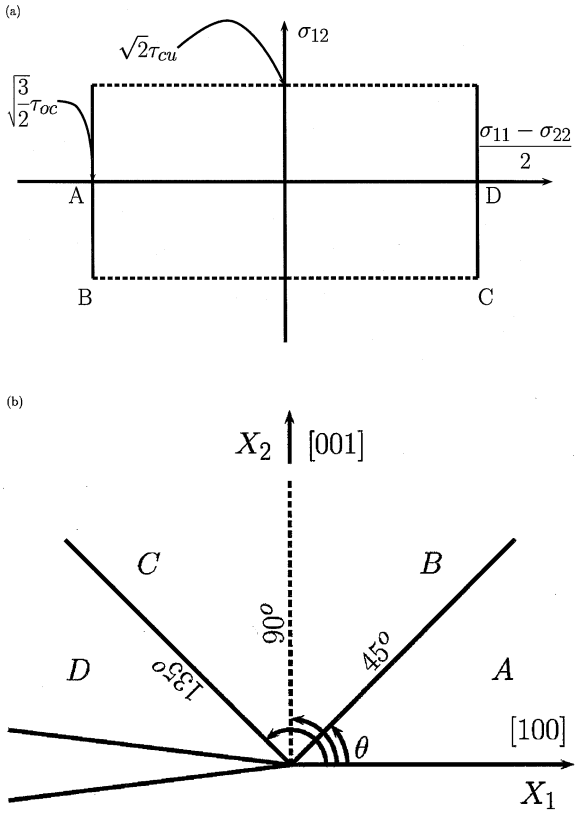

Figure 3. Structure of the crack tip field solution for the (001)[100] crack orientation, in the case $\tau_{cub}/\tau_{oc} < \sqrt{3}/2$: (a) yield surface, (b) sector boundaries, the rays with given angle θ correspond to stress discontinuity. The Cartesian components of the stress tensor are constant in the sectors labelled *A* to *D*. The yield surface edges and sector boundary corresponding to the activation of cube slip are in dashed lines.

2.3. Alternative solutions at the crack tip: slip vs. kink bands

Rice's solution for the near-tip stress field of a stationary crack, and its extensions, is by no means the only possible one. It assumes that the stresses are at yield at all angles about the crack tip. Drugan (2001) explores alternative solutions that exclude kink-type shear bands at the crack tip in elastic-ideally plastic crystals. This is possible provided that sub-yield near-tip sectors are introduced in which the material remains elastic. In the case of the (001)[110]

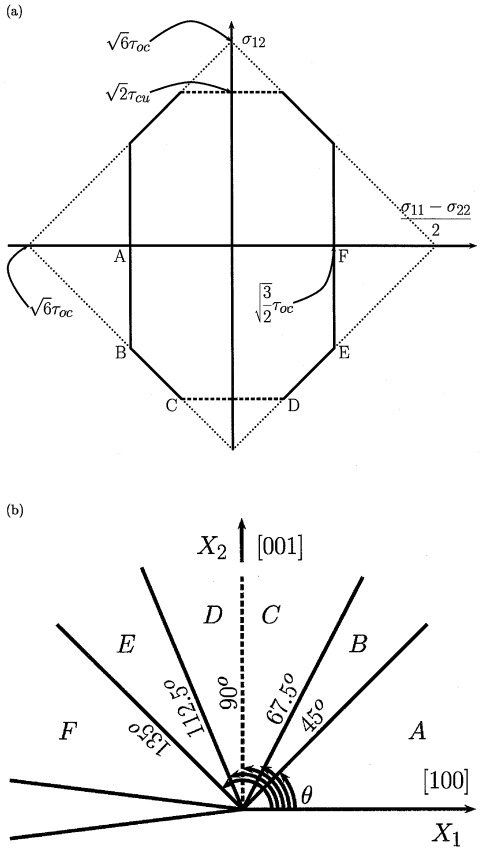

Figure 4. Structure of the crack tip field solution for the (001)[100] crack orientation, in the case $\sqrt{3}/2 < \tau_{cub}/\tau_{oc} < \sqrt{3}$: (a) yield surface, (b) sector boundaries, the rays with given angle θ correspond to stress discontinuity. The Cartesian components of the stress tensor are constant in the sectors labelled A to F. The yield surface edges and sector boundary corresponding to the activation of cube slip are in dashed lines.

Table 3. Stress values in the sectors around the tip of a stationary (001)[100] crack, in the case $\sqrt{3}/2 < \tau_{cub}/\tau_{oc} < \sqrt{3}$. The sector names are indicated in the corresponding Figure 4.

sector	σ_{11}	σ_{22}	σ_{12}
A	$(4-2\sqrt{2})\tau_{cu}+(3\sqrt{2}-2)\sqrt{3}\tau_{oc}$	$(4-2\sqrt{2})\tau_{cu}+(4\sqrt{2}-2)\sqrt{3}\tau_{oc}$	0
B	$(4-2\sqrt{2})\tau_{cu}+(5\sqrt{\frac{2}{3}}-2\sqrt{3})\tau_{oc}$	$(4-2\sqrt{2})\tau_{cu}+(7\sqrt{\frac{2}{3}}-2\sqrt{3})\tau_{oc}$	$-\sqrt{\frac{3}{2}}\tau_{oc}$
C	$(2-\sqrt{2})\tau_{cu}+(2\sqrt{2}-1)\sqrt{3}\tau_{oc}$	$(2-3\sqrt{2})\tau_{cu}+(4\sqrt{2}-1)\sqrt{3}\tau_{oc}$	$-\sqrt{2}\tau_{cu}$
D	$(2-\sqrt{2})\tau_{cu}+(2\sqrt{2}-1)\sqrt{3}\tau_{oc}$	$(2+\sqrt{2})\tau_{cu}-\sqrt{3}\tau_{oc}$	$-\sqrt{2}\tau_{cu}$
E	$3\sqrt{\frac{3}{2}}\tau_{oc}$	$\sqrt{\frac{3}{2}}\tau_{oc}$	$-\sqrt{\frac{3}{2}}\tau_{oc}$
F	$2\sqrt{\frac{3}{2}}\tau_{oc}$	0	0

crack in F.C.C. crystals, Drugan proposes at least two alternative solutions. The first one keeps the discontinuity line AB but modifies the frontiers of the three remaining sectors in order to ensure full stress continuity at these new radial boundaries, which requires one purely elastic sector. The second one admits two stress and strain jumps at 54.7° and 125.3°.

Two-dimensional Finite Element simulations of near–tip stress and strain fields agree with Rice's solution for stationary cracks (Cuitiño and Ortiz, 1992; Forest et al., 2001; Flouriot et al., 2003). It is not clear how the constraints on the type of discontinuity lines proposed in (Drugan, 2001) could be enforced in the numerical simulation. It seems then that it would not be possible to perform Finite Element computations including additional features of crystal plasticity like lattice rotation and work-hardening for this type of alternative solutions. In contrast, Rice's solution remains a good approximation of the numerical results even when finite strain and slight hardening are accounted for.

However, another way of controlling the magnitude of kink bands is to use strain gradient crystal plasticity models, with the advantage that it can be implemented numerically. Xia and Hutchinson (1996) argue that the strong strain gradients at the crack tip may affect the local material behaviour. They have worked out expressions of crack tip fields in isotropic strain gradient plasticity. In Forest et al. (2001), Finite Element computations of crack tip fields are presented within the framework of a Cosserat single crystal plasticity theory. It introduces explicit additional material hardening associated with the density of geometrically necessary dislocations or equivalently lattice curvature. When applied to an otherwise elastic-perfectly plastic crystal, this enhancement of classical continuum crystal plasticity affects mainly the intensity of kink bands that may form at the crack tip according to Rice's solution. If the additional hardening due to lattice curvature is high enough, the formation of kink bands can even be precluded. Discontinuity lines associated with pure slip are left unchanged. This difference between slip and kink bands in generalized crystal plasticity has also been underlined by Forest et al. (1998). The additional hardening parameter can be used to control the intensity of slip in kink bands. Note that simulations based on dislocation dynamics of the near-tip stress-strain field show that the intensity of found kink bands depends on the initial density of sources in the vicinity of the band (Van der Giessen et al., 2001).

Drugan's and Cosserat-based alternative solutions will be kept in mind for comparison with the experimental results provided in Section 5.

3. Finite element model and computational tools

3.1. Constitutive equations and Finite Element model

The formulation of finite strain crystal plasticity used in this work is that proposed by Mandel (1973), based on a multiplicative decomposition of the deformation gradient $\underset{\sim}{\mathbf{F}}$ into elastic and plastic parts:

$$\underset{\sim}{\mathbf{F}} = \underset{\sim}{\mathbf{E}}\underset{\sim}{\mathbf{P}}. \tag{10}$$

The assumption that pure plastic deformation $\underset{\sim}{\mathbf{P}}$ leaves the lattice undistorted and unrotated leads to the definition of an unique so-called isoclinic intermediate configuration. Lattice rotation is then defined as the rotation part in the polar decomposition of $\underset{\sim}{\mathbf{E}}$. Plastic flow is the result of the possible activation of N slip systems:

$$\dot{\underset{\sim}{\mathbf{P}}}\underset{\sim}{\mathbf{P}}^{-1} = \sum_{s=1}^{N} \dot{\gamma}^s \, \underline{\mathbf{l}}^s \otimes \underline{\mathbf{n}}^s, \tag{11}$$

where γ^s denotes the amount of slip according to system s. In the case of single crystal nickel-base superalloys, the number N is equal to 18 (12 octahedral and 6 cube slip systems, as in Section 2.2). The model includes the hyperelastic relation linking the Green–Lagrange elastic strain measure $\underset{\sim}{\mathbf{G}}$ defined on the isoclinic configuration to the corresponding Piola–Kirchhoff stress tensor $\underset{\sim}{\mathbf{S}}$:

$$\underset{\sim}{\mathbf{S}} = \rho_i \frac{\partial \Psi}{\partial \underset{\sim}{\mathbf{G}}} \tag{12}$$

$$\underset{\sim}{\mathbf{G}} = \frac{1}{2}(\underset{\sim}{\mathbf{E}}^T \underset{\sim}{\mathbf{E}} - \underline{\mathbf{1}}), \quad \underset{\sim}{\mathbf{S}} = \frac{\rho_i}{\rho} \underset{\sim}{\mathbf{E}}^{-1} \underset{\sim}{\boldsymbol{\sigma}} \underset{\sim}{\mathbf{E}}^{-T}. \tag{13}$$

The volume densities with respect to the current and intermediate configurations are respectively denoted by ρ and ρ_i. The elastic part of the free enery potential Ψ is taken as a quadratic form involving the matrix of elastic moduli which has its usual form when considered on the isoclinic configuration. A viscoplastic formulation of the flow rule is used in order to avoid possible indeterminacy in the activation of slip systems:

$$\dot{\gamma}^s = \mathrm{Max}\left(\left(\frac{|\tau^s| - \tau_c^s}{k} \right)^n, 0 \right) \mathrm{sign}\left(\tau^s\right), \tag{14}$$

where τ is the resolved shear stress and τ_c the threshold for plastic yielding according to the Schmid law. A rate-independent behaviour is obtained for high values of n and small values of k. Note that within the finite strain framework the resolved shear stresses τ^s is defined as

$$\tau^s = \underset{\sim}{\boldsymbol{\Sigma}} : (\underline{\mathbf{l}}^s \otimes \underline{\mathbf{n}}^s), \quad \text{with} \quad \underset{\sim}{\boldsymbol{\Sigma}} = \underset{\sim}{\mathbf{E}}^T \underset{\sim}{\mathbf{E}} \underset{\sim}{\mathbf{S}}, \tag{15}$$

where $\underset{\sim}{\boldsymbol{\Sigma}}$ is sometimes called the Mandel stress.

An implicit Newton integration scheme is used for solving the previous set of differential equations (Méric et al., 1991; Besson et al., 2001). The variational formulation of the boundary value problem according to an updated–Lagrangian scheme is discretized following the displacement-based Finite Element Method. The global nonlinear system is solved using a Newton scheme requiring local consistent tangent matrices. The reader is referred to (Simo and Hughes, 1997; Besson et al., 2001) for a detailed presentation of the resolution scheme and to the internet reference (Z-set package, 1996) for a description of the used Finite Element program. A small strain version of the model has been tested in the case of stationary crack problem by comparing the numerical solution with Rice's solution with very good agreement (Flouriot et al., 2003). When lattice rotation is introduced for elastic-ideally plastic crystals, the numerical solution differs from Rice's solution merely by the amount of glide in the localization bands radiating from the crack tip. Stronger differences have been found for hardening crystals (Mohan et al., 1992; Cuitiño and Ortiz, 1992).

3.2. Presentation of the samples and Finite Element mesh

The dimensions and detailed drawing of the Compact Tension specimen considered in this work are shown in Figure 5a. It is cut in a single crystal 40 mm × 38.4 mm plate with a

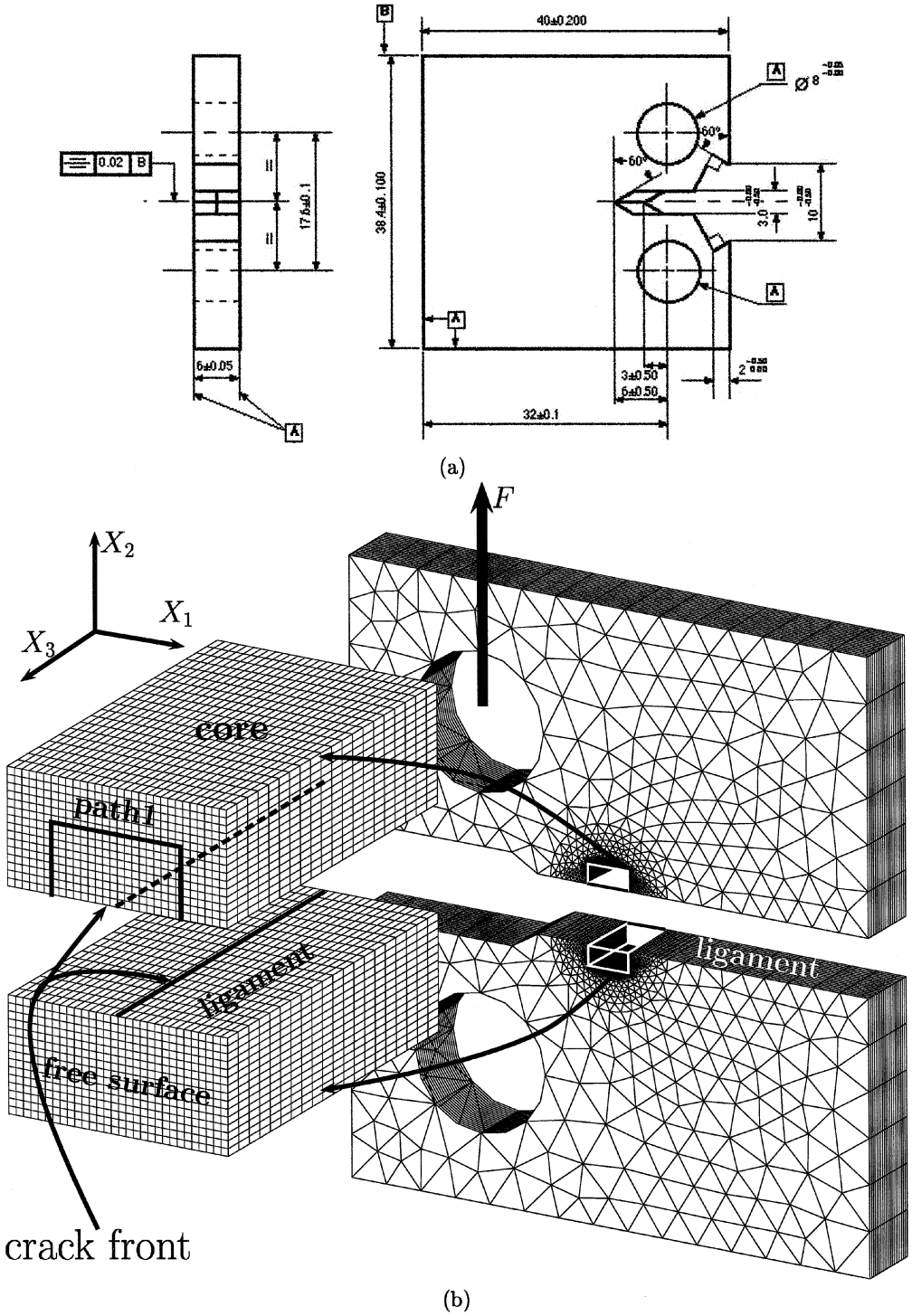

Figure 5. Compact Tension specimen: (a) specimen dimensions and geometry, (b) 3D Finite Element mesh, and close-up to the near-crack region. Zoom at the mesh domain called *core* in one half of the CT specimen. Upper and lower parts are separated for the illustration. This way of representation is used in the three following figures. The set of elements *core* is defined, with the line *path1*.

thickness $B = 6$ mm. The effective width of the specimen is $w = 32$ mm. The corresponding three-dimensional Finite Element mesh is given on the same Figure 5b, with a zoom at the fine mesh of the near-tip region. The crack tip region is made of a *disk* with a regular grid in the domain called *core*. The original CT specimen is fatigue pre-cracked, so that the crack length a can differ from specimen to specimen. The retained value for the computations is given at the end of this paragraph. One rectangular path is underlined along which stress or strain values will be plotted. The distance of *path1* from the crack tip are resp. $x_1 = 50$ μm, $x_2 = 50$ μm.

The three-dimensional mesh is deduced from a 2D one by 3 mm extension in direction 3. Only one quarter of the specimen is considered when ideal symmetric orientations are investigated. However, for comparison with exprimental results for which small deviations from ideal orientations have been measured, meshes of the entire specimen are also produced. Meshes with 2 to 20 layers of elements in the thickness are used. The elements are 20-node quadratic bricks and 15-node prismatic elements with full integration (27/18 Gauss points). For comparison, Cuitiño and Ortiz (1996) used six elements in the thickness of their 3D meshes of four-point bending specimens. These elements were quadratic in the plane and linear along the thickness.

Regarding boundary conditions, the ligament is fixed in direction 2 for ideally-oriented specimens. The point of application of the vertical load F is indicated in Figure 5b. This point cannot move in direction 1. For ideally-oriented specimens, the mid-section, i.e., the plane normal to direction 3 going through the center of the specimen, is fixed with respect to direction 3 whereas the free surface is left free of forces.

Throughout this work, the load F is prescribed to the sample. However it is easier to speak in terms of the corresponding imposed stress intensity factor K in order to compare different experiments. For the cubic single crystals considered, we adopt a simplified definition of the applied K factor. It is the stress intensity factor of the same specimen made of an elastic isotropic medium submitted to the same load F (the Young's modulus of AM1 in direction [001] is adopted in this convention). The relation between this definition of K and the load F has been parametrized based on Finite Element computations. It reads:

$$K = \frac{F}{Bw^{1/2}} \frac{2+\alpha}{(1-\alpha)^{3/2}} \left(0.886 + 4.64\alpha - 13.32\alpha^2 + 14.7\alpha^3 - 5.6\alpha^4\right). \tag{16}$$

The formula is valid for $0.2 \leq \alpha = a/w \leq 0.7$.

If not otherwise stated, all the specimens are loaded up to the load $K = 32$ MPa $\sqrt{\text{m}}$. which corresponds to a force of 3030 N for a crack length of 17.6 mm. This crack length $a = 17.6$ mm is taken for all presented computations. This value is close to the experimental one.

3.3. Influence of mesh type and element size

A regular grid is used at the crack tip but it has been checked that the use of a fan-like mesh as in (Cuitiño and Ortiz, 1996) does not affect the results provided that the number of elements is high enough.

The influence of the element size was investigated in the two-dimensional case. No significant effect was found on the stress distribution in the near-tip region. However the finer the mesh the higher the amount of slip at the crack tip and the thinner the width of the localisation bands, as shown in Figure 6a. Figure 6a shows the amount of equivalent slip γ_{eq} defined as

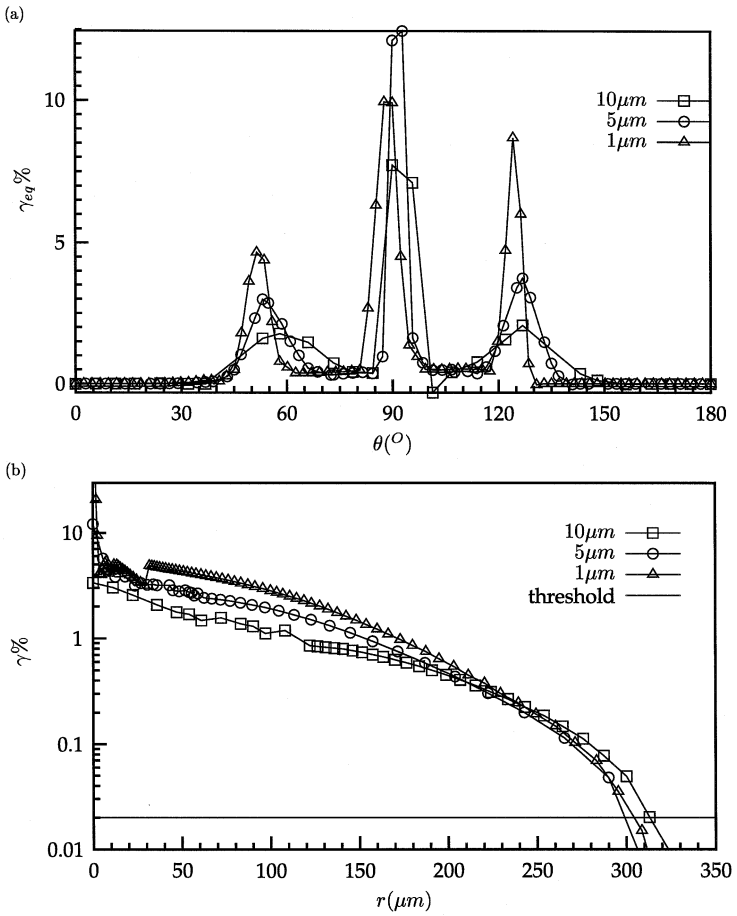

Figure 6. Comparaison of 2D Finite Element results for 3 different mesh sizes ((001)[110] crack orientation): (a) equivalent plastic slip along a circular arc at $r = 50$ μm; (b) activity of slip system (111)[$\bar{1}$01] along the localization band AB, defining the extension of the plastic zone.

$$\dot{\gamma}_{eq} = \sum_{s=1}^{N} |\dot{\gamma}^s|, \tag{17}$$

along *path1* at the crack tip (see the mesh of Figure 5). It appears that most of the plastic deformation takes place inside bands having the orientation of the discontinuity lines of Rice's solution. Plastic slip is almost zero in sectors A and D. The radius r of the plastic zone, defined as the distance from the crack tip inside localization bands at which plastic slip becomes smaller than a threshold value (here chosen as 2×10^{-4}), turns out to be almost mesh independent (Figure 6b). In the localization band AB this radius is about 320 μm.

The number of layers of elements in the thickness of the mesh has been increased until convergence of the local fields is obtained, i.e., a difference less than 1% between the results of two successive meshes. This leads to a number of 20 layers. The differences in the results near the crack tip between 2-element and 20-element thick meshes are illustrated in Figure 7. It can be seen that the vertical plastic zone above the crack tip cannot be captured by the coarse mesh.

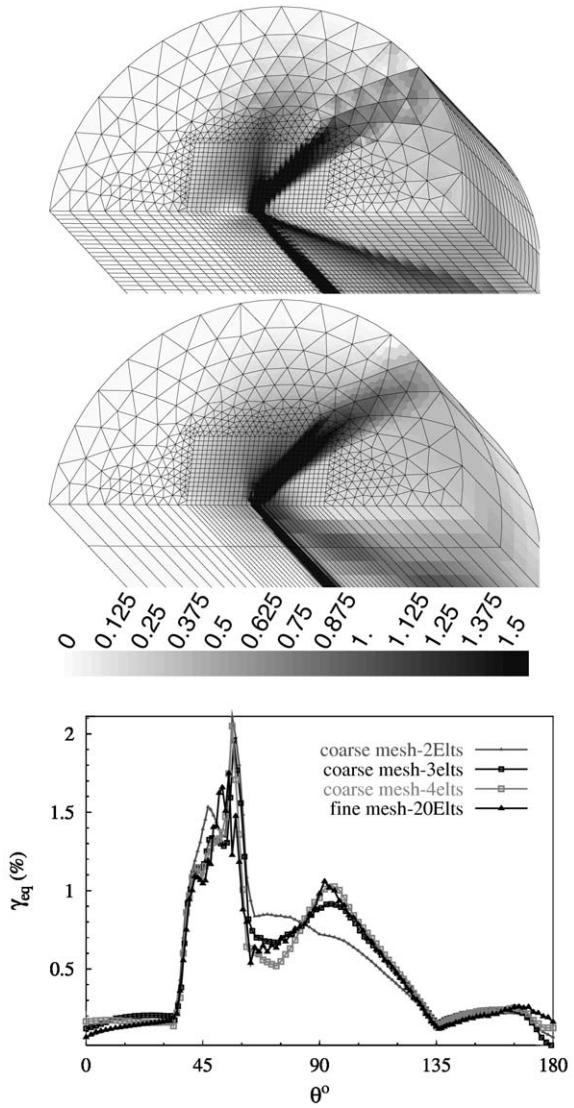

Figure 7. Effect of the number of elements in the thickness of the sample on the strain localization pattern at the free surface in the mesh domain *disk*: 20 quadratic elements (top) and two quadratic elements (middle). The strain values in the color scale are in per cent. The equivalent plastic slip is plotted along the line *path1* around the crack (see Figure 5) for different numbers of elements within the thickness (bottom).

3.4. PARALLEL COMPUTING METHOD

For the three-dimensional problem to be solved in reasonable computer time, it has been resorted to parallel computing. The obtained three-dimensional Finite Element meshes lead to a huge amount of degrees of freedom. The resolution of the corresponding linear system requires very large memory and disk storage capacity. The local integration of the evolution equations for the internal variables is very time-consuming. Parallel computing is a powerful tool now widely available in structural mechanics. The parallelized Finite Element code used in this work (Z-set package, 1996) resorts to the subdomain decomposition method called FETI (Finite Element Tearing and Interconnecting method (Farhat and Roux, 1991)). It is

based on a decomposition of the considered structure into subdomains that can share only interfaces. Each subdomain is handled by one different processor. Parallel solving of local integration of constitutive equations is therefore automatic, provided that the information at an integration point is sufficient for the integration of the variables at this point (local constitutive equations). The subdomains are fixed at the beginning. At the global level, the independent resolution on a given subdomain leads to discontinuities of the global solution at interfaces. The FETI method is a dual iterative method that distributes the forces at the interfaces for the displacement field to become continuous. One simply mentions here the three main steps of the computation, after the decomposition of the structure into subdomains: resolution of the sub-problems into each domain, iterative scheme to get the solution of the global problem, and merging the results of all subdomains. Subdomains are automatically produced by an algorithm that tries to minimize the surface of common interfaces. A sparse matrix solver is used for the resolution for each subdomain.

The total number of degrees of freedom in the 20-element thick mesh of the CT specimen, defined as the number of nodes multiplied by the 3 components of the displacement vector, is about 270 000. The whole 3D mesh has been decomposed into six subdomains. The amount of memory required for each processor is about 750 Mo (mainly used for the storage of the stiffness matrix for each subdomain). The time for the computation of one entire specimen up to the considered maximum load is about 10 hours while using 6 nodes of a PC cluster (Pentium III–600 MHz).

4. Three-dimensional F.E. analysis of single crystal CT specimens

The results of 3D Finite Element simulations of CT specimens under monotonous loading are now presented for three different crack orientations. In this section, ideal crack orientations only are considered. The computations have been performed twice : with octahedral slip systems only on the one hand, and taking both octahedral and cube slip into account, on the other hand. The material parameters used are for AM1 at room temperature (see Table 1). The figures in this section show the results of the computation with octahedral slip only. Comments on the differences arising when cube slip is introduced are given in the text.

The numerical results are presented successively for the three considered crack orientations: (001)[110], (110)[001] and (001)[100]. Two guidelines are followed: the comparison between the near-tip fields obtained at the free surface and in the mid-section of the specimens, on the one hand, and the analysis of other three-dimensional effects observed ahead of the crack tip on the other hand. Figures 8–10 deal with the surface/mid-section comparison. For better comparison, the inner and outer disks are put together in a symmetric way. A quantitative comparison is drawn by plotting the equivalent amount of slip along *path1* on the outer surface, in the mid section. Rice's reference solution is also plotted to measure how much the inner and outer fields depart from the pure plane strain solution. Figures 11–13 give a broader view of the three-dimensional near-tip plastic strain fields. For that purpose, a special representation of the 3D fields is adopted as explained in Figure 5b: the elements of the mesh domain called *core* only are represented for the upper part of the specimen but also for the symmetrical lower part. This makes the free surface of the specimen and four internal surfaces visible, which is necessary to get a 3D view of the plastic strain field. Both parts are separated from each other in order to show the horizontal plane containing the crack front. These two parts are placed in space always in the same way as indicated in Figure 5b.

All the figures are shown at the same final applied load $K = 32$ MPa $m^{1/2}$. The quantity mapped in all these figures is the equivalent plastic slip measure defined by Equation (17). The same color scale is used for all contour plots of equivalent plastic slip in this work. It is the scale given in Figure 7. The values of γ_{eq} found inside the strain localization bands described below generally vary from 5 to 15%. Outside the bands, they remain below 1%.

4.1. (001)[110] CRACK

The structure of the localization bands radiating from the crack tip in the mid-section is in agreement with the reference plane strain solution (see Figures 8a and 8b). The intensity of slip inside the bands in the mid–section in the 3D computation almost coincides with that found by a 2D computation. This is no longer true at the free surface where a vertical band dominates. One single slip system is mainly active in this vertical band ($(1\bar{1}1)[110]$). This slip system is also activated in the vertical kink band of the mid-section field. The fact that only one system dominates in the vertical band at the free surface means that the surface does not remain plane and that the band induces out-of-plane deformation at the surface.

Looking now at the whole 3D crack tip region of Figure 11, one sees the transition from the mid-section to the outer structure of the plastic strain field. The whole structure is more complex and fully three-dimensional. An additional strain localization plane can be seen that is not expected in the planar analysis and where the slip system $(1\bar{1}1)[\bar{1}01]$ is the main active system. This produces more plastic strain in front of the crack tip in the mid section than predicted by the 2D analysis (see Figure 8).

4.2. (110)[001] CRACK

In the mid-section of the specimen where symmetry conditions are enforced, the structure of the three discontinuity lines expected in Rice's analysis is retrieved in the form of three bands of more intense plastic slip (see Figures 9a and 9b). However the intensity of the vertical band is much lower than expected. Furthermore, a fourth band can be seen at $\theta = 35°$ where the slip system $(11\bar{1})[011]$ is triggered. In contrast, at the free surface two strain localization bands only are visible. The vertical one is due to the single slip system $(1\bar{1}1)[\bar{1}10]$.

Note that the vertical band does not cross the entire section of the specimen, it deviates rather from the free surface as can be seen from Figure 12. In contrast, the band inclined at about 55° crosses the whole width of the specimen. At the free surface in the inclined band, the systems $(111)[\bar{1}01]$ and $(111)[0\bar{1}1]$ are mainly activated. The slip system $(111)[0\bar{1}1]$ dominates however, which results again in out-of-plane plastic flow at the free surface. On the horizontal section containing the crack front, a localization band forms a V-shape ahead of the crack, due to the activation of slip system $(1\bar{1}1)[011]$. It has the structure of a kink band. This shows the highly three–dimensional structure of the strain field in the near-tip region.

The computation including both octahedral and cube slip provides a similar picture of the 3D near-tip field. The vertical band in the mid-section and at the free surface are due to the activation of one single cube slip system.

4.3. (001)[100] CRACK

Three bands only are obtained in the mid-section of the (001)[100] cracked specimen, out of the four expected ones for this orientation from the 2D analysis. They have the expected

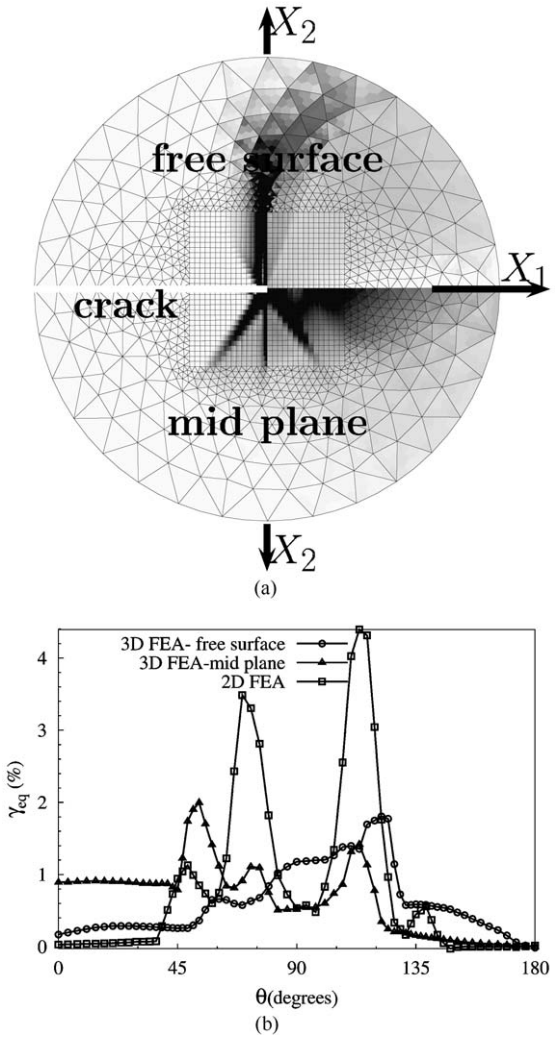

Figure 8. Comparison of the equivalent plastic slip fields at the free surface and in the mid-section of the specimen ((001)[110] crack orientation): (a) Symmetric maps representing the free surface (top) and the mid-plane (bottom). The color scale is the same as in Figure 7. (b) Plot of γ_{eq} along *path1* at the free surface, in the mid-plane and in a two-dimensional analysis.

structure and orientation but highly attenuated intensity when compared to the planar analysis (Figures 10a and 10b).

At the free surface, almost all slip systems are activated and contribute to more homogeneous strain distribution around the crack tip than for the previous orientations. Figure 13 again shows the three-dimensional structure of the near-tip fields in a CT specimen. It shows a lower tendency to strain localization than the two previous orientations. Surprisingly, at the free surface, plastic strain is also localized in a band located behind the crack tip. It was not the case in the previous orientations for which bands are observed ahead of the crack or normal to the crack plane. In contrast, in the mid-plane the band inclined at about $\theta = 45°$ is the dominant one.

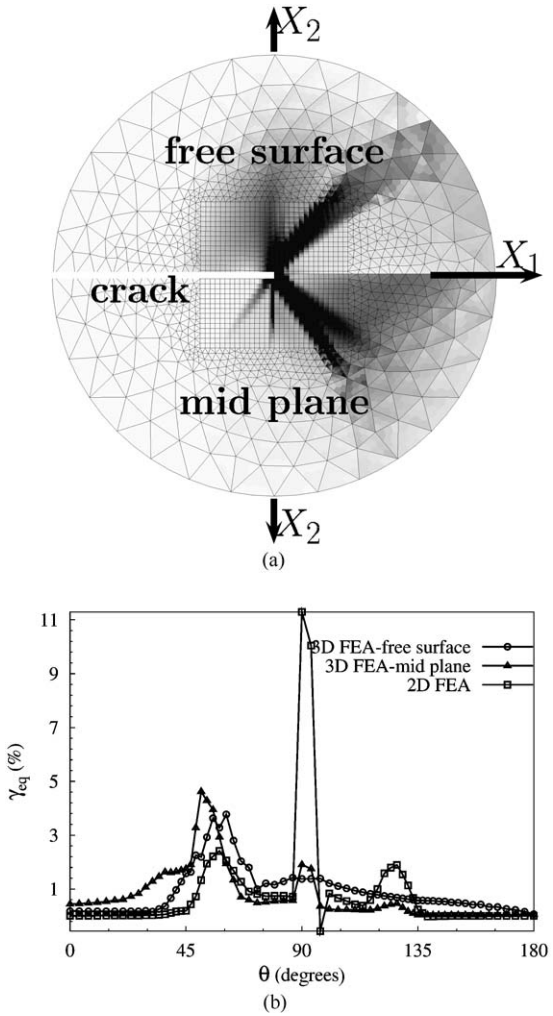

Figure 9. Comparison of the equivalent plastic slip fields at the free surface and in the mid-section of the specimen ((110)[001] crack orientation): (a) Symmetric maps representing the free surface (top) and the mid-plane (bottom). The color scale is the same as in Figure 7. (b) Plot of γ_{eq} along *path1* at the free surface, in the mid-plane and in a two-dimensional analysis.

The introduction of cube slip systems attenuates the strain localization patterns even more. The cube slip systems contribute mainly in a rather vertical sector above the crack tip.

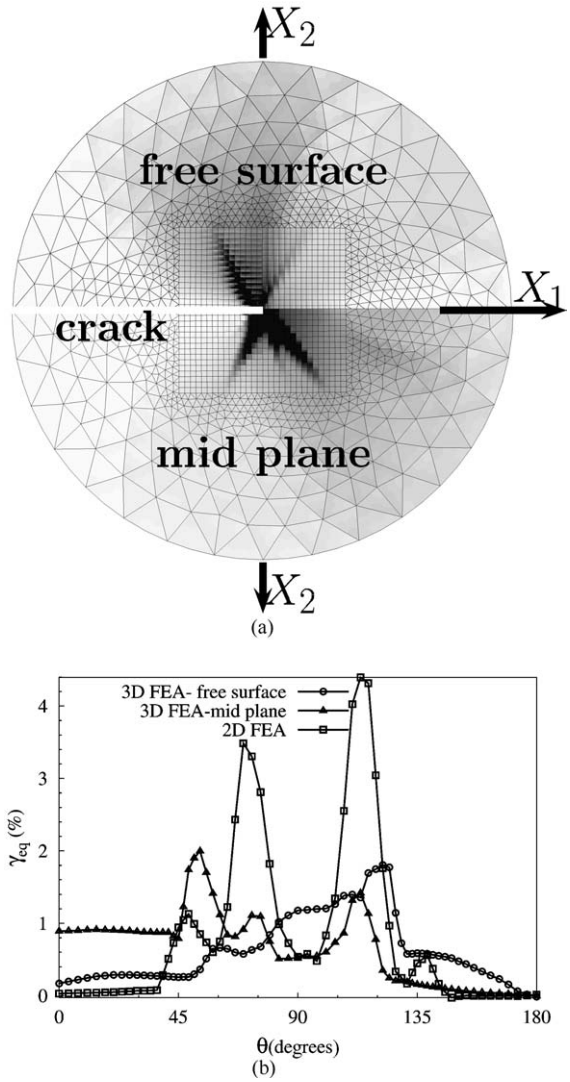

Figure 10. Comparison of the equivalent plastic slip fields at the free surface and in the mid-section of the specimen ((001)[100] crack orientation): (a) Symmetric maps representing the free surface (top) and the mid-plane (bottom). The color scale is the same as in Figure 7. (b) Plot of γ_{eq} along *path1* at the free surface, in the mid-plane and in a two-dimensional analysis.

5. Experimental results

5.1. Experimental procedure

Tests were carried out on three CT specimens having the dimensions and geometry given in Figure 5. Two different orientations could be tested : two specimens close to (110)[001] crack orientations, and one specimen close to (001)[100] crack orientation. The specimen lattice orientations were checked using X-ray Laue back-reflexion. The real crystal orientations deviate by maximum 4° from the ideal ones. The free surfaces of the specimens was polished down to 1 μm diamond finish on both sides. Tests were conducted on a servo-hydraulic SCHENCK testing machine under load control (100 kN load capacity). The amplitude of

the stress intensity factor K was computed from the experimentally determined crack length a from Equation (16).

Specimens were precracked at 650 °C using a sine wave loading at a frequency of 10 Hz with a ratio $R = K_{\max}/K_{\min} = 0.1$, with $K_{\max} = 10$ MPa m$^{1/2}$. The stress intensity factor $K_{\max}$ was progressively reduced in steps in such a way that the final $K_{\max}$ was as low as possible. During pre-cracking, crack length was measured using optical microscopy. In addition the crack length was monitored continuously throughout the pre-cracking procedure using a potential drop technique. The final crack length was about 17 mm for all three samples. After precracking, specimens were polished again.

The actual test consists in applying a monotonous tensile load on the cracked specimen at room temperature. The applied load is chosen such that the crack does not propagate significantly during the test. The free surfaces of the specimens were then examined by optical and scanning electron microscopy (SEM) after unloading. Finally, each specimen is polished again in order to obtain a surface as planar as possible for EBSD (Electron Back-Scattered Diffraction) analysis on the free surface. Several crystal orientation maps were obtained in the crack tip region, with a minimum resolution of one spot at every 2 μm. The precision of the measured lattice orientation at each spot is better than 1°.

5.2. (110)[001] CRACK

Two specimens with crack orientations close to (110)[001] have been tested: the first test was conducted up to an intermediate load $K = 15$ MPa m$^{1/2}$, and the second one up to the final load $K = 32$ MPa m$^{1/2}$. The first crack did not propagate whereas the second one propagated over a small distance of 10 μm. A SEM view of the crack tip region of specimen 1 and an optical micrograph for specimen 2 are given in Figure 14a. At the intermediate load (specimen 1), two fine arrays of slip lines are already visible arranged in two main strain localization bands at about $\theta = \pm 54°$. The most numerous slip lines are perpendicular to the direction of the localization band, which suggests the formation of a kink band. The pure kink band expected from Rice's analysis is the sum of the contributions of two slip systems sharing the same slip plane : $(111)[10\overline{1}]$, $(111)[01\overline{1}]$. The present experiment shows that one of them at least is activated, but one cannot be sure that both are activated from optical or SEM micrographs alone. A second slip system is also activated mainly inside the lower localization band. The same bands are visible in specimen 2 that has undergone twice the load of specimen 1, with the same arrays of fine slip lines (Figure 14b). Two additional slip line bundles can be seen ahead of the crack tip. The slip lines were interpreted as traces of (111) and $(11\overline{1})$ planes, as shown on the same figure. It means that the slip plane activated in the upper kink plane is also present in the lower slip band. The reverse is true for the traces of $(11\overline{1})$ plane. Vertical lines are also visible just below the crack tip in specimen 2. The corresponding slip plane cannot be identified unambiguously: the vertical lines can be traces of octahedral or cube planes. No slip lines were observed behind the crack tip. The extension of the plastic zone does no seem to be larger than 300 to 400 μm, based on the optical microscopy observations.

The EBSD analysis at the free surface shown in Figure 16a (specimen 2) reveals that lattice rotation has taken place inside both kink bands. The green color corresponds to the reference orientation taken as the initial one. The map shows the distribution of lattice rotation angle with respect to axis 3 (normal to the specimen free surface) in yellow-red color for counterclockwise rotation and blue for clockwise rotation. It has already been noticed that, in

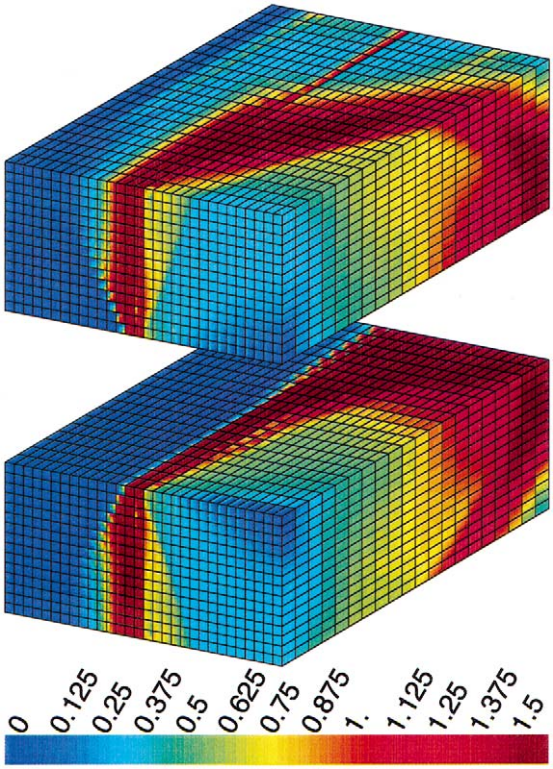

Figure 11. Three-dimensional equivalent plastic slip field near the crack tip for the (001)[110] crack orientation. The front planes correspond to the free surface. The adopted way of representation is explained in Figure 5b.

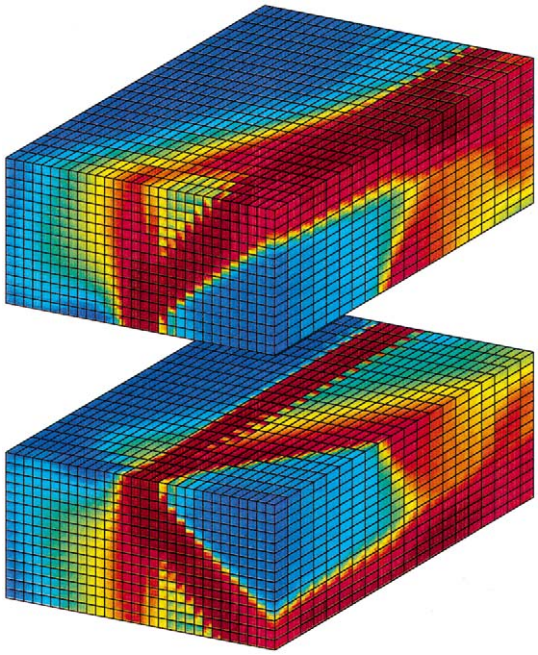

Figure 12. Three-dimensional equivalent plastic slip field near the crack tip for the (110)[001] crack orientation. The front planes correspond to the free surface. The color scale is the same as in Figure 11.

contrast to slip bands, kink bands are associated with lattice rotation (Forest et al., 2001). In fact, two parallel yellow lines can be seen on the EBSD map. This is to be related to the fact that the crack has grown slightly during the test by an amount of about 10 μm. The first kink band on the left is revealed by the EBSD analysis and could not be observed unambiguously by optical microscopy. On can infer from the EBSD observation that the kink band does not develop during crack growth but forms when the crack stops. This is in accordance with Rice and Drugan's comments that stress discontinuity lines cannot move normal to itself in quasistatically growing crack (Drugan and Rice, 1994; Rice, 1987). The maximum amount of measured lattice rotation is 5°.

5.3. (001)[100] CRACK

The test on the (001)[100] cracked specimen was performed up to the load $K = 35$ MPa m$^{1/2}$ without observed crack growth. Two main localization bands can be seen on the SEM micrograph of the final state of the near-tip region in Figure 15b. Additional slip lines almost normal to the previous ones are present in the sectors neighbouring the localization bands. In each case, the observed slip lines can be traces of two possible slip planes ($(\overline{1}11)$ or $(11\overline{1})$ on the one hand, and (111) or $(1\overline{1}1)$, on the other band). No slip lines can be seen behind, nor vertically above or below the crack tip.

The EBSD analysis of the lower part of the crack tip region reveals lattice rotation in a band in front of the crack tip, in a vertical one and also behind (Figure 16b). The first blue band only can be related to the presence of slip line bundles. Maximal values of 3° lattice rotation are found inside the vertical band.

6. Discussion

The objective of the discussion is to draw a comparison between the numerical and experimental results obtained is this work, with respect to two main points of view: a qualitative one, namely the comparison of the orientation and structure of computed and observed strain localization bands, and a quantitative one, namely direct comparison of amount of lattice rotation around the crack tip.

6.1. INFLUENCE OF FATIGUE PRECRACKING

There is an important difference between the conditions of the Finite Element computation and that of the experiments. The tests are carried out on fatigue pre-cracked specimens, whereas the simulations are made on virgin specimens. It is known that fatigue cracking leaves a plastic zone in the track of the crack that may influence further crack growth. Before a direct comparison of the presented numerical and experimental results of this work, the assumption of neglecting this plastic wave in the Finite Element computation must be tested. For that purpose, a two-dimensional simulation of fatigue crack growth has been performed up to the final crack length a used for the monotonous test. The simulation is based on the technique of successive node release at the crack tip at given instants (here every third cycle). The sample orientation considered here is (110)[001]. The resulting plastic strain field is shown in Figure 17. Figure 17a gives the map of the γ_{eq} variable. At the maximum load of the first cycle, the structure of three localization bands arises as expected. It can still be seen on the left of Figure 17a. In Figure 17b (respectively, 17c), the contribution of the slip systems activated

in the band AB (respectively, BC) only is plotted. At the final crack tip, one sees only the band AB in front of the crack tip whereas the vertical one has not formed. Once the crack has reached the wanted length, the simulation is continued by subjecting the specimen to monotonous loading up to $K = 30$ MPa $m^{1/2}$. The final plastic strain field at the crack tip is shown in Figure 17d. The expected three intense strain bands are retrieved, including the vertical one and the one behind the crack tip. The profile of equivalent plastic slip does not significantly differ then from the one found for the virgin specimen (Figure 8b).

This simple simulation suggests that, due to the high intensity of the monotonous load, the history of pre-cracking at the crack tip can be neglected in the present case.

6.2. Slip system activity and localization bands

For comparison, the discontinuity lines of the 2D analytical solution are superimposed on the micrographs of the crack tip region at the free surface for the specimens (110)[001] and (001)[100] in Figures 18 and 19. It appears that the strain localization bands observed experimentally coincide with predicted discontinuity lines, except the slip line bundles of the (110)[001] crack that rather belong to a sector. However all the predicted discontinuity lines are not apparent on the free surface of the specimens. More generally, all observed slip traces are in accordance with numerical and analytical solutions. However, all predicted slip systems are not seen. It must be noted that slip lines are present in the experiment only when the corresponding Burgers vector has a high enough out-of-plane component. The strain localization band at $\theta = 54°$ has been identified as a kink in both computation and experiment. The computation predicts the activation of the two slip systems that are necessary to form a pure kink. In fact only one of them (namely $(111)[01\bar{1}]$) dominates at the free surface according to the simulation. This is probably the slip system responsible for the slip traces seen in the experiment.

It must be noted that the observed near-tip region is very different from that observed in single crystal aluminium, copper or copper alloys which have the same crystallographic structure as AM1. Near notches in copper single crystal specimens, slip traces are seen mainly inside angular sectors, even though some sectors remain sometimes free of traces (Shield, 1996; Crone and Shield, 2001; Crone and Drugan, 2001). This is due to the fact that copper exhibits a strong hardening behaviour whereas the single crystal nickel-base superalloy considered in this work remains almost elastic ideally-plastic. This makes the studied situation closer to that investigated in (Rice, 1987). Rice's solution predicts stresses lying on the yield surface in the found sectors. This amount of slip actually taking place in each sector then strongly depends on the material response, hardening or not. The Finite Element analysis predicts indeed a low amount of plastic slip outside the intense strain band (rarely more than 0.6%, while it is always above 1.5% inside the bands). The order of magnitude of the computed size of the plastic zone as defined in Section 3.3 is in good agreement with the experimental results. It is also in accordance with available data on the extension of plasticity at the crack tip measured by Crompton in single crystal superalloy MAR-M200 at room temperature (Crompton and Martin, 1984).

A good agreement is reached between experiment and computation for the (110)[001] crack orientation. This can be seen by comparing the micrograph of Figure 14b with the equivalent plastic slip field predicted at the free surface by the 3D Finite Element computation (Figure 12). The predicted localization band inclined at about $\theta = 54°$ and a vertical band are both observed on the deformed specimen, even though the computation overestimates

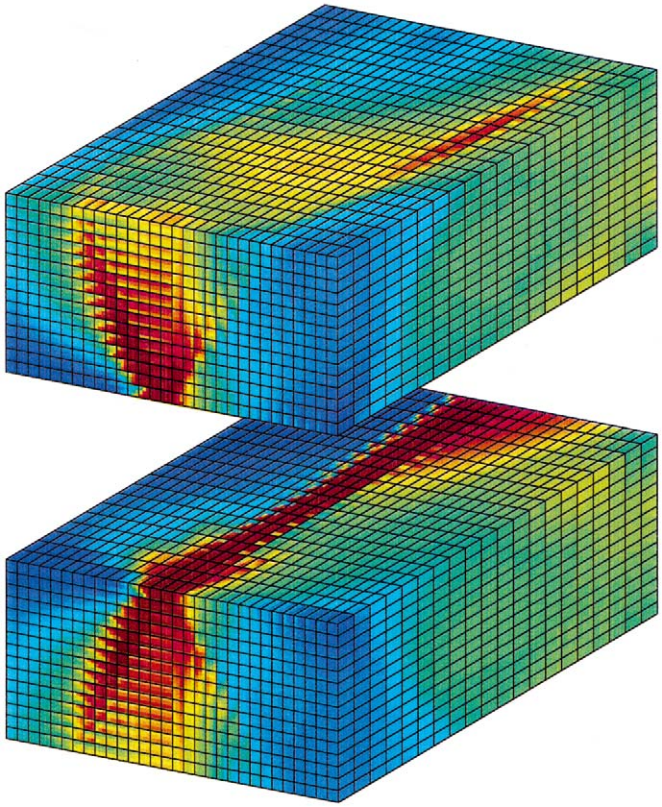

Figure 13. Three-dimensional equivalent plastic slip field near the crack tip for the (001)[100] crack orientation. The front planes correspond to the free surface. The color scale is the same as in Figure 11.

the vertical band. Closer agreement with experiment can be reached by introducing a better description of the constitutive behaviour of AM1 at room temperature, and the actual specimen orientation found by X-ray Laue back-reflexion. In particular, slight isotropic hardening can be added to the model (Méric et al., 1991). If the actual orientation of the sample is introduced, no symmetry remains in the boundary value problem and a mesh of the entire CT specimen was considered. The new equivalent plastic slip map at the free surface is shown in Figure 20. The large localization band in front of the crack tip is still there but the vertical band found for the ideal orientation is now strongly attenuated. The shape of the deformation zone is in much better agreement with the observations. The activated slip systems are the same as in the experiment.

In the case of the (001)[100] crack orientation, the agreement between computation and experiment is less clear (compare Figures 13 and 19). In particular, the vertical band and the plastic zone behind the crack tip predicted by the Finite Element analysis are not observed in the optical nor SEM micrographs. However the EBSD analysis of Figure 16b shows that lattice rotation takes place at the location of the expected deformation bands. Indeed, the Finite Element computation confirms that these band are associated with lattice rotation. The vertical band is due to cube slip according to the computation (see also Figure 4). Additional tests are needed to give a more definitive answer.

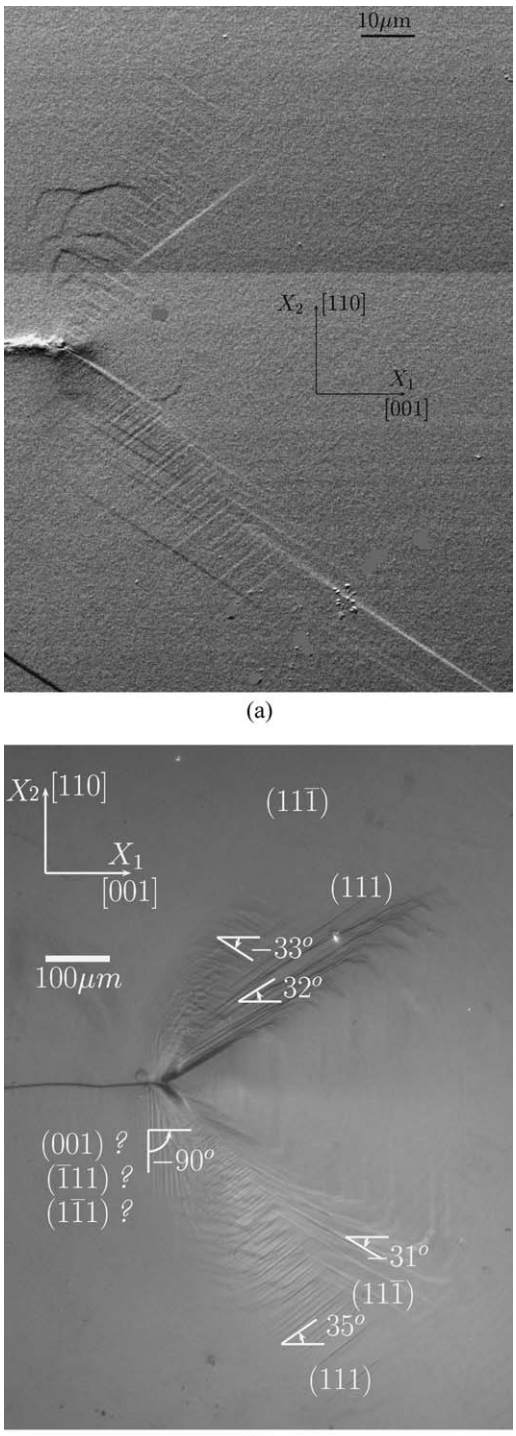

Figure 14. Experimental observations of the crack tip region for the (110)[001] crack orientation: (a) SEM micrograph of specimen 1, (b) optical micrograph of specimen 2. The orientation and identification of slip lines are given.

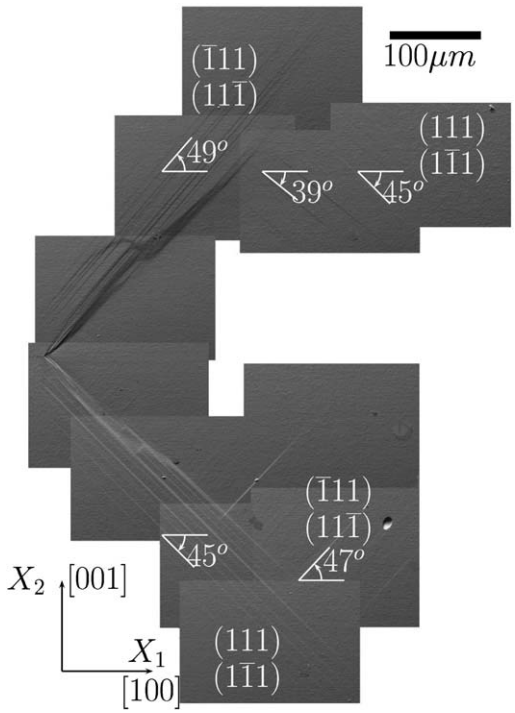

Figure 15. SEM micrograph of the crack tip region for the (001)[100] crack orientation. The orientation and identification of slip lines are given.

6.3. Out-of-plane deformation and crack tip opening

Confocal microscopy has been used to measure the out-of-plane deformation at the free surface of the (001)[100] CT specimen. The magnified thickness reduction in front of the crack tip is shown in Figure 21a. One system dominates($(111)[01\bar{1}]$) at the free surface, which is responsible for the out-of-plane deformation schematically drawn in Figure 21b. The corresponding Burgers vector makes an angle of 45° with respect to the initial free surface. The Finite Element simulation strongly underestimates the found thickness reduction.

6.4. Lattice rotation

EBSD analyses provide quantitative information about lattice rotation induced by plasticity around the crack tip, that can be directly compared with finite element results. In continuum crystal plasticity, lattice rotation is accounted for by the rotation part in the polar decomposition of elastic deformation $\underset{\sim}{\mathbf{E}}$ (Equation (10)). This information is stored at each integration point at each loading step. Let us consider the rectangular circuit drawn on the EBSD map of Figure 16a and plot the absolute value of the rotation angle with respect to axis 3 at the end of the test. The same circuit can be drawn on the finite element mesh at the free surface. The corresponding rotation angle found at the nodes along this circuit in the simulation is plotted on the same graph for comparison (Figure 22). It can be seen that the computation predicts accurately the location where lattice occurs and the amount of lattice rotation. The existence

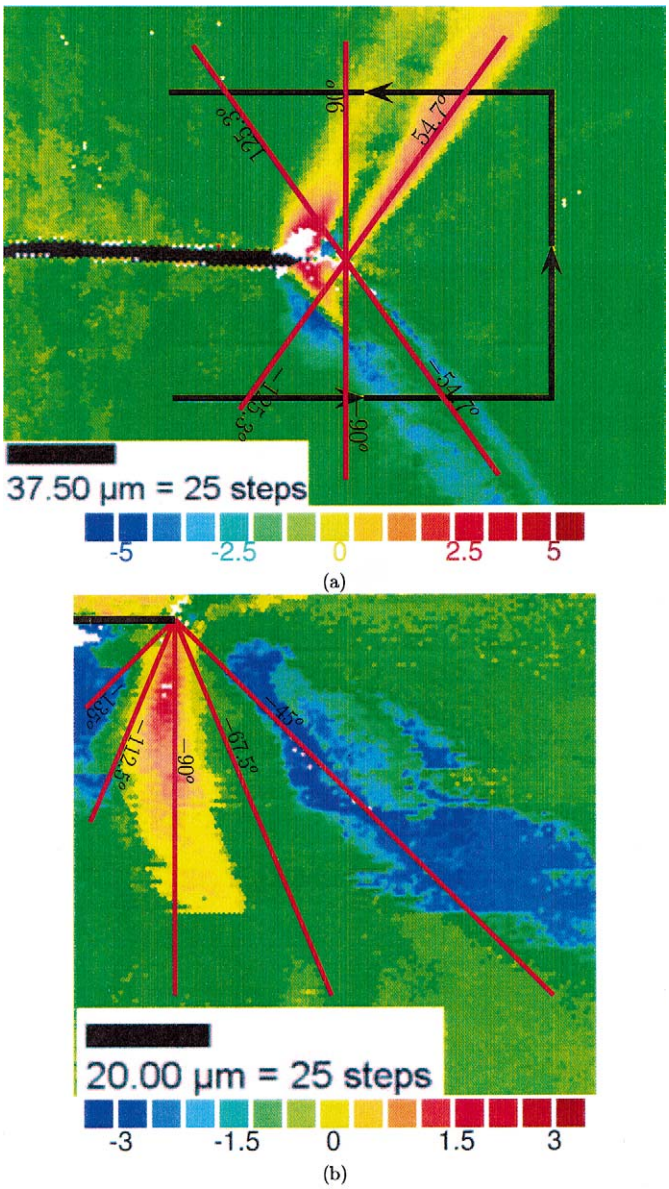

Figure 16. EBSD analysis of the near-tip region on the free surface: (a) (110)[001] crack orientation, (b) (001)[100] crack orientation. The discontinuity lines found in the planar solution of the corresponding crack problem have been superimposed for comparison.

of lattice rotation confirms the kink character of the deformation band that the finite element computation is able to capture.

7. Conclusions

Numerical simulations based on classical continuum crystal plasticity theory are able to capture many features of near-crack tip deformation modes in elastoplastic single crystals, provided that the full three-dimensional aspects of plastic deformation are taken into account. In particular, the analytical solutions that have been worked out under plane strain conditions are useful

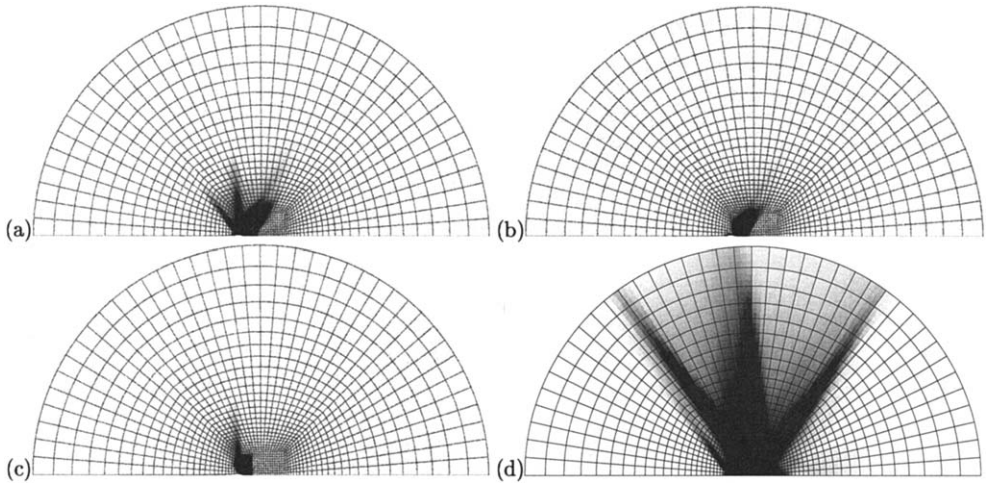

Figure 17. Simulation of fatigue crack growth by the node release method ((001)[110] crack orientation): (a) map of equivalent plastic slip after propagation, (b) map of plastic slip corresponding to the slip systems activated in the band AB, (c) map of plastic slip corresponding to the slip systems activated in the band BC, (d) map of equivalent plastic slip when the pre-cracked sample is loaded again monotonously.

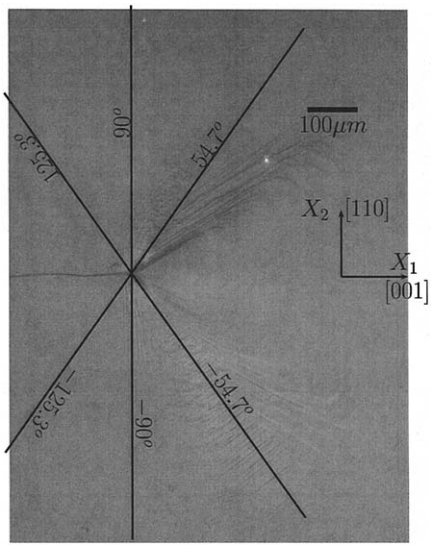

Figure 18. Superimposed experimental view of the (110)[001] crack and discontinuity lines according to Rice's solution.

for a first assessment of the near-tip region fields but they cannot be directly compared with the structure of the crack tip fields in computational nor experimental analysis of CT specimens. The 3D Finite Element computations even show that the comparison with the fields found in the core of the specimen is not entirely satisfactory.

The specific material used in this work, a single crystal nickel-base superalloy, displays an elastic almost ideally-plastic behaviour at room temperature, that allows in principle for a direct comparison with analytical solutions for the structure of the near-tip fields. For that purpose, specific asymptotic solutions have been worked out that take both octahedral and cube

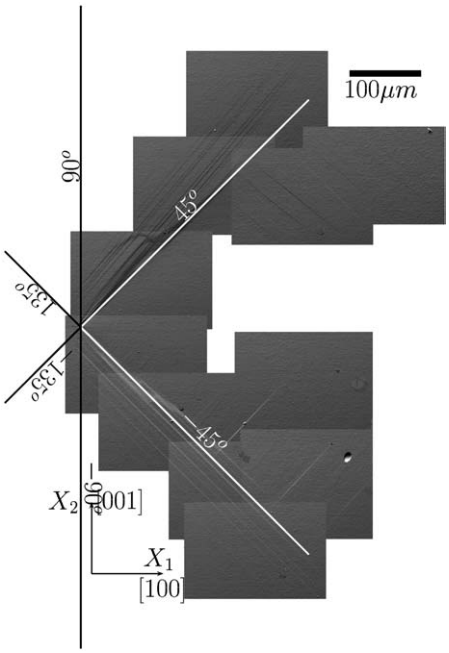

Figure 19. Superimposed experimental view of the (001)[100] crack and discontinuity lines according to Rice's solution.

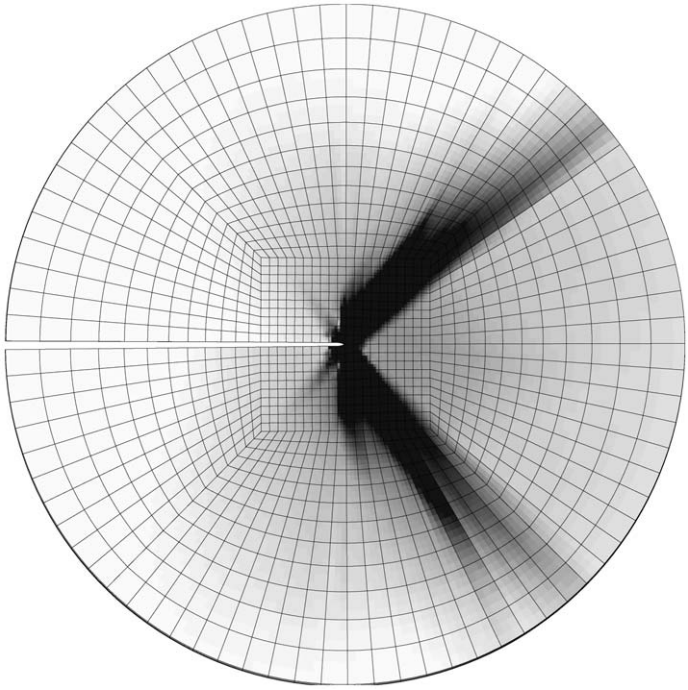

Figure 20. Three-dimensional Finite Element computation of the crack tip field at the free surface taking a slightly hardening constitutive behaviour of AM1 and the real orientation of specimen 2 (near-(110)[001] crack orientation) into account: map of equivalent plastic slip. The color scale is the same as in Figure 7.

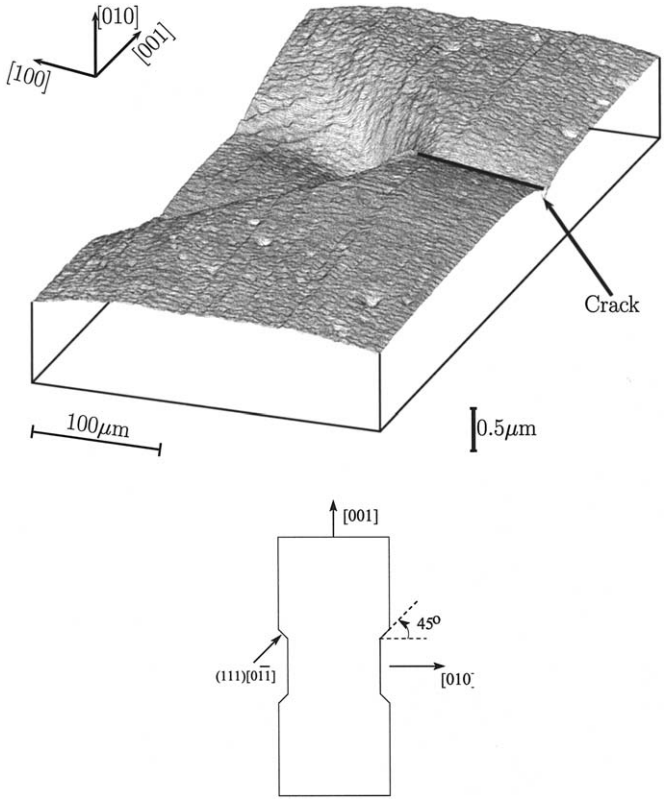

Figure 21. Experimental view of out-of-plane deformation of the (001)[100] crack obtained by confocal microscopy. The out-of-plane deformation is due to the (111)[0$\bar{1}$1] slip system.

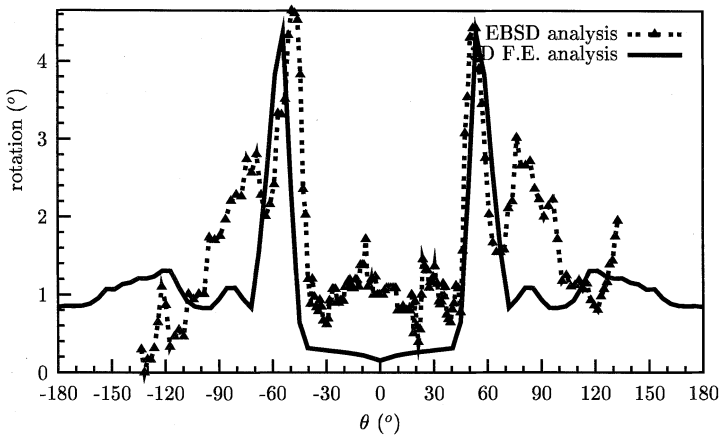

Figure 22. Experimental and computed profiles of lattice rotation around axis 3 along the path indicated in Figure 16a ((110)[001] crack orientation).

slip that can exist in this material. Structures involving 3, 4 or even 5 discontinuity lines have been presented. In the experimental results, there is only one possible evidence of cube slip at the crack tip, namely the vertical slip lines observed on the (110)[001] specimen. However, the identification of actual slip plane responsible for these traces remains ambiguous.

Strain localization bands have been mainly observed at the crack tip of the three investigated CT specimens, instead of the usual sectors full of slip lines observed in hardening crystals like copper. Experimental evidence of kink banding at the crack tip in two specimens has been provided, confirmed by quantitative comparison between EBSD analysis and Finite Element results.

The plastic strain fields predicted by the 3D Finite Element analyses are highly three-dimensional and strongly orientation-dependent. The strain field computed at the free surface is significantly different from the internal one. Furthermore, planes of intense deformation have been found that are not parallel nor perpendicular to the specimen free surface or mid-section. They can build a V-shape deformation pattern ahead of the crack tip. The plastic strain maps shown in this work can be used in the future for comparison with experimental work on other elastic ideally-plastic single crystals.

Further experimental analysis is necessary for a better comparison between computational and experimental results. In particular, strain field measurements are the best-suited tools. Measurements of the out-of-plane displacement have been briefly reported. The use of regular fiducial grids could also provide quantitative information about in-plane deformation. In the case of nickel-base superalloys, extensions of the proposed methodology to the study of crack tip viscoplasticity at higher temperature also is an important issue for future work.

Accordingly, in the present case, alternative solutions as proposed in (Drugan, 2001) or even higher order crystal plasticity as in (Forest et al., 2001) do not seem to be needed. However, additional quantitative measurements like in-plane strain field measurements are necessary to conclude on this issue. Improvements in the agreement between Finite Element results and experimental observations and measurements could be gained by extending continuum crystal plasticity models. Generalized crystal plasticity theories may also be needed for the modeling of subsequent crack growth.

The precise description of crack tip deformation behaviour proposed in this work is in fact the necessary step for proper understanding and modeling of subsequent crack growth under monotonous or fatigue loading. This is the main incentive for future work. However, an important limitation of continuum crystal plasticity is the discrete nature of the deformation events observed at the crack tip: intense discrete lines instead of strictly continuous plastic slip. Taking these important features of crystal plasticity into account lies within the realm of dislocation dynamics, which has already proved to be a relevant tool for analysing crack tip fields and even subsequent growth (Van der Giessen et al., 2001; Deshpande et al., 2001).

References

Arakere, N. and Swanson, G. (2002). Effect of orientation on fatigue failure of single crystal nickel base turbine blade superalloys. *J. Eng. Mat. for Gas Turbines and Power* **134**(1), 161–176.

Asaro, R. (1983). Crystal plasticity. *J. Appl. Mech.* **50**, 921–934.

Aswath, P. (1994). Effect of orientation on crystallographic cracking in notched nickel-base superalloy single crystal subjected to far-field cyclic compression. *Met. Mat. Trans* **25A**, 287–297.

Besson, J. Cailletaud, G., Chaboche, J.-L. and Forest, S. (2001). *Mécanique non linéaire des matériaux*, Hermès, France, 445 p.

Bettge, D. and Osterle, W. (1999). Cube slip in near [111] oriented speciments of single crystal nickel-base superalloys. *Scripta Mat.* **40**(4), 389–395.

Cho, J. and Yu, J. (1991). Near-crack-tip deformation in copper single crystals. *Phil. Mag. Letters* **64**(4), 175–182.

Crompton, J. and Martin, J. (1984a). Crack growth in a single-crystal superalloy at elevated temperatures. *Metall. Trans.* **15A**, 1711–1719.

Crone, W. and Drugan, W. (2001). Comparison of experiment and theory for crack tip fields in ductile single crystals. In: *Proceedings of the ICF 10 International Congress on Fracture* (Edited by K.K. Ravi-Chander, B. Karihaloo, T. Kishi, R. Ritchie, A. Yokobori Jr. and T. Yokobori).

Crone, W. and Shield, T. (2001). Experimental study of the deformation near a notch tip in copper and copper-beryllium single crystals. *J. Mech. Phys. Solids* **49**, 2819–2838.

Cuitiño, A. and Ortiz, M. (1992). Computational modeling of single crystals. *Modelling Simul. Mater. Sci. Eng.* **1**, 225–263.

Cuitiño, A. and Ortiz, M. (1996). Three-dimensional crack-tip fields in four-point-bending copper single-crystal specimens. *J. Mech. Phys. Solids* **44**, 863–904.

Defresne, A. and Rémy, L. (1990). Fatigue behavior of CMSX2 superalloy [001] single crystals at high temperature II: Fatigue crack growth. *Mat. Sci. and Eng.* **A129**, 55–64.

Deshpande, V., Needleman, A. and Van Der Giessen, E. (2001). A discrete dislocation analysis of near threshold fatigue crack growth. *Acta Mater.* **49**, 3189–3203.

Drugan, W. (2001). Asymptotic solutions for tensile crack tip fields without kink-type bands in elastic-ideally plastic single crystals. *J. Mech. Phys. Phys. Solids* **49**, 2155–2176.

Drugan, W. and Rice, J. (1984). Restrictions on quasi-statically moving surfaces of strong discontinuity in elastoplastic solids. In: *Mechanics of Material Behavior* (Edited by G. Dvorak and R. Shield), Elsevier, Amsterdam, 59–73.

Farhat, C. and Roux, F.-X. (1991). A Method of Finite Element Tearing and Interconnecting and its Parallel Solution Algorithm. *Int. J. for Numerical Methods in Engineering* **32**, 1205–1227.

Fleury, E. (1991). Endommagement du superalliage monocristallin AM1 en fatigue isotherme et anisotherme. Ph.D. thesis, Ecole Nationale Supérieure des Mines de Paris.

Flouriot, S., Forest, S. and Rémy, L. (2003). Strain localization phenomena under cyclic loading: Application to fatigue of single crystals. *Computational Materials Science* **26**, 61–70.

Forest, S. (1998). Modeling Slip, Kink and Shear Banding in Classical and Generalized Single Crystal Plasticity. *Acta Materialia* **46**(9), 3265–3281.

Forest, S., Boubidi, P. and Sievert, R. (2001). Strain localization patterns at a crack tip in generalized single crystal plasticity. *Scripta Mat.* **44**, 953–958.

Forest, S., Olschewski, J., Ziebs, J. Kühn, H.-J., Meersmann, J. and Frenz, H. (1996). The elastic/plastic deformation behaviour of various oriented SC16 single crystals under combined tension/torsion fatigue loading. In: *Sixth International Fatigue Congress* (Edited by G. Lütjering and H. Nowack), ASME, STP, 139–150.

Garrett, G. and Knott, J. (1975). Crytallographic fatigue crack growth in aluminium alloys. *Acta Metall.* **23**, 841–848.

Gilman, J. (1955). Structure and polygonization of bent zinc monocrystals. *Acta Metall.* **3**, 277–288.

Gupta, V. (1993). Tensile crack-tip fields in elastic-ideally plastic hexagonal crystals and layered materials. *Acta Metall.* **16**, 553–561.

Hanriot, F., Cailletaud, G. and Rémy, L. (1991). Mechanical behavior of a nickel-base superalloy single crystal. In: *Proc. of Int. Conf. on High Temperature Constitutive Modeling* (Edited by A. Freed and K. Walker), ASME, STP, 139–150.

Henderson, M. and Martin, J. (1996). The influence of crystal orientation on high temperature fatigue crack growth of a Ni-based single crystal superalloy. *Acta Mat.* **44**(1), 111–126.

Köster, A. and Rémy, L. (2000). An oxidation creep-fatigue damage model for fatigue at high temperature and under thermal transients. In: *Fatigue ' 99* (Edited by H. Sehitoglu and H. Maier), Elsevier, pp. 2139–2144.

Kysar, J. and Briant, C. (2002). Crack tip deformation fields in ductile single crystals. *Acta Mat.* **50**(9), 2367–2380.

Lerch, B. and Antolovich, S. (1990). Fatigue crack propagation behavior of a single crystalline superalloy. *Metall. Trans. A* **21A**, 2169–2177.

Leverant, G. and Gell, M. (1975). The influence of temperature and cyclic frequency on the fatigue fracture of cube oriented nickel-base superalloy single crystals. *Metall. Trans. A* **6A**, 367–371.

Mandel, J. (1973). Equations constitutives et directeurs dans les milieux plastiques et viscoplastiques. *Int. J. Solids Structures* **9**, 725–740.

Méric, L., Poubanne, P. and Cailletaud, G. (1991). Single crystal modeling for structural calculations: Part 1-Model presentation. *J. Eng. Mat. Techn.* **113**, 162–170.

Mohan, R., Ortiz, M. and Shih, C. (1992). An analysis of cracks in ductile single crystals-II Mode I loading. *J. Mech. Phys. Solids* **40**(2), 315–337.

Neumann, P. (1974). New experiments concerning the slip process at propagating fatigue cracks-I. *Acta Met.* **22**, 1155–1165.

Nouailhas, D. and Cailletaud, G. (1995). Tension-torsion behavior of single-crystal superalloys: experiment and finite element analysis. *International Journal of Plasticity* **11**(4), 451–470.

Nouailhas, D., Pacou, D., Cailletaud, G. Hanriot, F. and Rémy, L. (1993). Experimental study of the anisotropic behaviour of the CMSX2 single crystal superalloy under tension-torsion loadings. In: *Advances in Multiaxial Fatigue* (Edited by D. McDowell and R. Ellis), 244–258.

Pan, J. (1986). Plain strain crack-tip stress field for anisotropic perfectly-plastic materials. *J. Mech. Phys. Solids* **34**, 617–635.

Rémy, L. and Skelton, R. (1992). In: *High Temperature Structural Design, ESIS 12* (Edited by M. Larsson), Mechanical Engineering Publications, London, 283–315.

Rice, J. (1987). Tensile crack tip fields in elastic-ideally plastic crystals. *Mechanics of Materials* **6**, 317–335.

Rice, J., Hawk, D. and Asaro, R. (1990). Crack tip fields in ductile single crystals. *Int. J. Fracture* **42**, 301–321.

Saeedvafa, M. and Rice, J. (1989). Crack tip singular fields in ductile crystals with Taylor power-law hardening; II: Plane strain. *J. Mech. Phys. Solids* **37**(6), 673–691.

Shield, T. (1996). An experimental study of the plastic strain fields near a notch tip in a copper single crystal, during loading. *Acta Mater.* **44**(4), 1547–1561.

Shield, T. and Kim, K.-S. (1994). Experimental measurement of the near tip strain field in an Iron-silicon single crystal. *J. Mech. Phys. Solids* **42**(5), 845–873.

Simo, J. and Hughes, T. (1997). *Computational Inelasticity*, Springer-Verlag, Berlin.

Van der Giessen, E., Deshpande, V., Cleveringa, H. and Needleman, A. (2001). Discrete dislocation plasticity and crack tip fields in single crystals. *J. Mech. Phys. Solids* **49**, 2133–2153.

Xia, Z. and Hutchinson, J. (1996). Crack tip fields in strain gradient plasticity. *J. Mech. Phys. Solids* **44**, 1621.

Z-set package (1996). www.nwnumerics.com, www.mat.ensmp.fr.